Superconducting Nanowire Single-Photon Detectors on Aluminum Nitride Photonic Integrated Circuits

by

Di Zhu

Submitted to the Department of Electrical Engineering and Computer Science
in partial fulfillment of the requirements for the degree of

Master of Science in Electrical Engineering and Computer Science

at the

MASSACHUSETTS INSTITUTE OF TECHNOLOGY

February 2017

Signature redacted

Author .....
Department of Electrical Engineering and Computer Science
January 31, 2017

Certified by Signature redacted .....
Karl K. Berggren
Professor of Electrical Engineering
Thesis Supervisor

Accepted by .. Signature redacted .....
Professor Leslie A. Kolodziejski
Chair, Department Committee on Graduate Students

Superconducting Nanowire Single-Photon Detectors on Aluminum Nitride Photonic Integrated Circuits

by

Di Zhu

Submitted to the Department of Electrical Engineering and Computer Science
on January 31, 2017, in partial fulfillment of the
requirements for the degree of
Master of Science in Electrical Engineering and Computer Science

Abstract

With recent advances in integrated single-photon sources and quantum memories, on-chip integration of high-performance single-photon detectors becomes increasingly important. The superconducting nanowire single-photon detector (SNSPD) is the leading single-photon counting technology for quantum information processing. Among various waveguide materials, aluminum nitride (AlN) is a promising candidate because of its exceptionally wide bandgap, and intrinsic piezoelectric and electro-optic properties. In this Master's thesis, we developed a complete fabrication process for making high-performance niobium nitride SNSPDs on AlN, and demonstrated their integration with AlN photonic waveguides. The detectors fabricated on this new substrate material have demonstrated saturated detection efficiency from visible to near-IR, sub-60-ps timing jitter, and ~6 ns reset time. This work will contribute towards building a fully integrated quantum photonic processor.

Thesis Supervisor: Karl K. Berggren
Title: Professor of Electrical Engineering

Acknowledgments

This thesis would not have been possible without the help from my professors, colleagues, friends, and families. In particular, I would like to thank:

My advisor, Professor Karl K. Berggren, for taking me as his student. His enthusiasm for science, dedication to education, enormous experience, and remarkable intuition have made him my role model in research.

Professor Dirk R. Englund for sharing his knowledge on quantum photonics. It is a pleasure to work with such a brilliant scientist.

Hyeongrak Choi (Chuck) and Tsung-Ju Jeff Lu for collaborating on this project. Chuck designed the PICs and built the setup for optical coupling. Jeff developed the fabrication process for AlN PICs. I am lucky to have them as my good friends in life as well.

Faraz Najafi for helping me start my research in the group, and teaching me all the nanofabrication skills.

Qing-Yuan Zhao, Andrew Dane, Francesco Bellei, and Adam McCaughan for always willing to share with me their experience and skills.

Lucy Archer, Emily Toomey, Ignacio Estay Forno, Corey Cleveland, Chung-Soo Kim, Navid Abedzadeh, and Richard Hobbs for their assistance and fruitful discussions.

Tim Schroeder and Eric Bersin from the Quantum Photonics Lab for helping me use their experimental setup.

All past and present members in the Quantum Nanostructures and Nanofabrication group.

Jim Daley and Mark Mondol for their help and expertise on fabrication.

My parents, who can always appreciate my thoughts, and inspire me with their wisdom.

My wife, Luying Li, and her family for their constant support.

Contents

List of Figures

List of Tables

Chapter 1

Introduction

This chapter first introduces the basics of superconducting nanowire single-photon detectors, including detection mechanism, detector metrics, system architecture, and materials; then describes the motivation, objective, and outline of this thesis.

1.1 Superconducting Nanowire Single-Photon Detectors

Superconducting nanowire single-photon detectors (SNSPDs, or SSPDs) outperform other single-photon counting technologies in many detector metrics, especially at the infrared wavelength [1]. SNSPDs play a key role in various applications, including deep-space communication, astronomical observation, and optical quantum information processing. Their advance in recent years has enabled significant progress in these fields, e.g., quantum key distribution over kilometer distance [3], NASA's Lunar Laser Communication Demonstration [4], and notably, the loop hole-free test of local realism [5], which ended the 80-year-long debate of quantum reality.

In this section, some basics about SNSPDs are described, including its working mechanism, basic properties, and system architectures.

1.1.1 Detection mechanism

Though the SNSPDs have been studied for more than a decade since their first demonstration in 2001 by Gol'tsman et al. [6], their detection mechanism is still under debate [7, 8, 9]. Here, without delving into the detailed microscopic processes, I will give a simple and intuitive description for the detection mechanism, as described in the original Gol'tsman paper.

An SNSPD is usually made of ~4-nm-thick, ~100-nm-wide superconducting nanowire, meandered into a square or circular shape. Figure 1-1 shows an scanning electron micrograph (SEM) of a standard 3 μm× 3μm niobium nitride (NbN) SNSPD. The bends are designed to follow an optimal curve that avoids current crowding [10]. To detect photon, the nanowire is DC-current biased slightly below its critical current, above which the superconducting nanowire switches to resistive state. When the nanowire is superconducting, there is no voltage across the nanowire. If a photon hits the nanowire and gets absorbed, its energy is deposited on the nanowire and creates a localized hotspot. Now, the bias current has to bypass the hotspot and causes current density around the hotspot to exceed the local critical current density. This chain reaction then switches the entire cross section into resistive state.[1] The bias current flowing through the resistive region starts to generate heat and further expands the hotspot. With the formation of resistance, voltage appears across the nanowire. The voltage pulse is registered using external readout electronics, and indicates a photon-arrival event.

1.1.2 Detector metrics

Single-photon detectors are evaluated based on their detector metrics. The most basic ones include detection efficiency, counting rate, dark-count rate, and jitter. Figure 1-2 compares the detector metrics among the four major single-photon detecting technologies at telecommunication wavelength. Depending on applications, other metrics

[1]Here, the hotspot is described as a normal domain. This interpretation is referred as "normal-core hotspot model." Though there has been an increasing criticism about this model [7], it is intuitive and gained great success in modeling the macroscopic device operation.

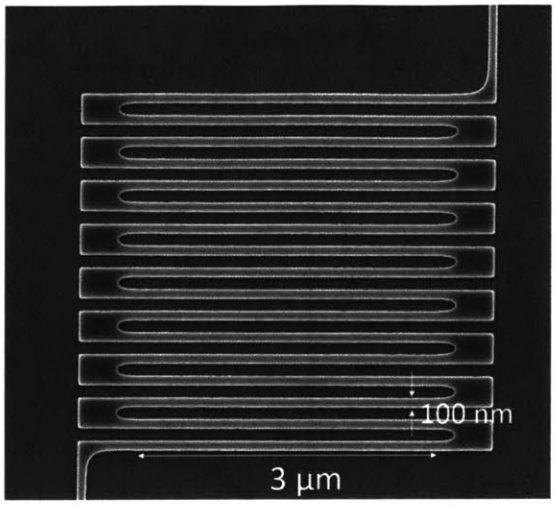

Figure 1-1: Scanning electron micrograph (SEM) of a standard 3 μm×3 μm SNSPD.

may also be important, e.g., photon-number and photon-energy resolution, operating temperature, array size, etc. SNSPDs have demonstrated near-unity detection efficiency, GHz counting rate, sub-1-cps dark count, and sub-20-ps timing jitter. Though these metrics have been demonstrated independently, it is difficult to have a single detector that possesses all the superior metrics simultaneously, and there may exist intrinsic tradespace among them.

Detection efficiency (DE). Detection efficiency refers to the probability of registering an electrical pulse when a photon arrives. In general, the system detection efficiency (SDE) follows the relation [11]:

$$SDE = \eta_c A \eta_i$$

where η_c is the optical coupling efficiency, A is the absorption rate, and η_i is the internal quantum efficiency of the detector. In the literature, device detection efficiency ($DDE = A\eta_i$) is very often reported. This is because the DDE is regarded an intrinsic property of the detector chip (calculated as counting rate/photon rate on the active area of the detector), while optical coupling (η_c) can be engineered externally with precise optical alignment.

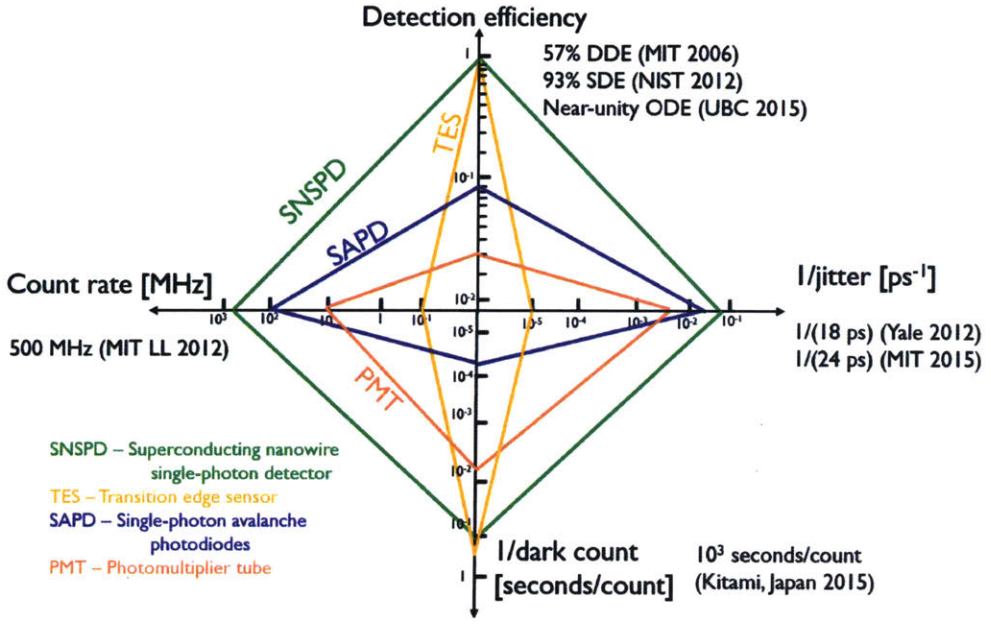

Figure 1-2: Comparing the detector metrics among major single-photon counting technologies at telecommunication wavelength. The data for TES, SAPD, and PMT are from [1], published in 2009. The original radar map was from Donald Winston.

To date, the highest reported SDE is 93%, which is from a fiber-coupled single-photon detector system made of amorphous tungsten silicide [12]. On waveguide-integrated systems, near-unity on-chip detection efficiencies have been shown [13].

Maximum count rate. An SNSPD normally operates at a free-running mode, where no external reset has to be performed.[2] After the detector fires, it will not be able to count photon until it resets to superconducting state. The reset time is determined by the L/R constant of the detector, where L is the kinetic inductance of the detector, which is proportional to the size of the detector, and R is the load impedance, which is set by the 50 Ω readout circuitry [15].

A typical large-area detector (e.g., 15 μm in diameter) has a reset time of 20 – 40 ns, and a small-area detector can have reset time of a few ns. Recently, sub-ns reset time has been demonstrated in sub-micron-long SNSPDs embedded in an optical waveguide cavity [16]. Another way to reduce nanowire inductance and reset time

[2]Gated mode is also demonstrated to enhance counting rate [14].

is to cascade nanowires in parallel, an architecture called "superconducting nanowire avalanche photodetector (SNAP)" [17].

Dark-count rate. Dark-count rate refers to how often the detector fires without a photon input. This parameter sets the signal-to-noise ratio for optical measurement. The dark counts come from two parts: background count (from stray light, thermal radiation, and electrical noise, etc.), and intrinsic dark count (from the intrinsic fluctuation in the current-carrying superconducting nanowire). The SNSPDs have low intrinsic dark count (10^{-4} cps with bandpass filter from [18]; 1 count every 8 hours measured on UV SNSPDs at JPL, unpublished), and no afterpulsing effect, which is common in the semiconductor single-photon avalanche detectors.

Timing jitter. Timing jitter is the uncertainty of the time interval between photon absorption and electrical pulse generation. The jitter limits how accurately one can determine the arrival time of a photon. It plays an important role in measuring photon correlations, determining the spatial resolution in LIDAR systems, etc.

The SNSPDs have a typical jitter of < 60 ps [19].[3] Some contributing factors have been identified, e.g., the slew rate and noise of the electrical pulse (electrical jitter), and geometry of the detector (geometric jitter) [20, 21]. Apart from these external aspects, the intrinsic jitter, which is related to the fundamental photo-excitation dynamics in the superconductor, is still hidden. Some fundamental questions include how exactly a photon excites quasi-particles in the superconductor, how the quasi-particles relax and switch the nanowire. These physical processes may have buried significant contribution of the timing uncertainties. The lack of understanding on the detailed detection process is currently preventing us from pushing the jitter to single-digit ps, or sub-ps level.

[3] SNSPDs made of amorphous superconductors (e.g., WSi) are found to have a larger jitter than those made of polycrystalline superconductors, e.g., NbN and NbTiN [12].

1.1.3 Optical coupling

Photons can be coupled to SNSPDs through three main schemes: optical fiber coupling, free-space coupling, and waveguide coupling.

Fiber coupling is the mainstream coupling method [22, 23, 24]. In fiber-coupled systems, the detector active area has to match the output optical mode of the fiber. A typical single mode fiber at telecommunication wavelength (e.g., SMF 28) has a physical core diameter of 8.2 μm and a mode diameter of 10.4 μm. To have a decent mode overlapping, the diameter of the SNSPDs needs to be at least 15 μm, which is considered large area and requires demanding fabrication yield. The benefit of fiber-coupled SNSPDs is that no window is required on the cryostat, which greatly reduces thermal load and background light. Fiber-coupled systems are also relatively stable. Now, fiber-coupled high-efficiency detectors have been commercialized, and most of them are using the NIST/JPL packaging technique [23, 24, 12] with WSi detectors.

Free-space-coupled SNSPD systems are useful for mid-IR communication, communication between moving platforms, gas spectroscopy, etc. [25] These systems require sophisticated alignment and filtering.

Recently, waveguide-integrated SNSPDs have attracted increasing interest [26, 27, 28, 29, 30, 31, 32]. Waveguide-integrated SNSPDs absorb light evanescently, so they are also called traveling-wave detectors. These detectors can achieve high optical absorption with a small size, which generally gives faster speed, lower jitter, and higher yield. The waveguide-integrated detectors are essential components for large-scale linear optical quantum computing (LOQC) systems [33].

1.1.4 Material systems

Detector material. Two main categories of superconducting materials are being used for SNSPDs. One is polycrystalline superconductor, e.g., NbN and NbTiN. These materials have relative high critical temperature (T_c). For example, NbN has a bulk T_c of 16 K, and thin-film (4-6 nm) T_c of 8-12 K, depending on deposition condition. The other emerging category of SNSPD material is amorphous superconductor,

e.g, WSi and MoSi [12, 34]. Though these materials have lower T_c, they have better film uniformity over large area, high fabrication yield, and large bias margin [12]. High fabrication yield is crucial for developing scalable detecting systems (e.g., large detector array) and commercializing the technology.

Substrate material. For polycrystalline superconductors, growing on a lattice-matched crystalline substrate will improve the film quality, and is believed to yield better devices. Therefore, the early NbN-based detectors are primarily grown on MgO and sapphire. To produce high quality film on amorphous substrate, e.g., SiO_2 and SiN_x, the deposition normally needs elevated temperature [35]. So far, SNSPDs have been fabricated on many technologically important substrates, e.g., Si [27, 13], SiN_x [35, 29], diamond [32, 31, 36], GaAs [26], and $LiNbO_3$ [37].

1.2 Towards Fully Integrated Photonic Quantum Processor

The superior performance of SNSPDs perfectly satisfies the demanding requirement for quantum optical measurements. With the significant progress of integrated photonics, solid-state single-photon emitter and quantum memories, a fully integrated photonic quantum processor is no longer elusive. Developing on-chip SNSPDs on suitable material systems will contribute towards achieving this ultimate goal. In this section, we describe the background, motivation, objective, and outline of this thesis.

1.2.1 Background and motivation

In optical quantum information science, on-chip integration has been a major effort in the past decade, because photonic integrated circuits (PICs) hold the promise of realizing large-scale quantum photonic processors. On a quantum PIC, besides single-photon sources and various passive waveguide elements, on-chip single-photon

detector is a critical element.

The SNSPDs are made of a single layer of superconducting material. This structural simplicity allows SNSPDs to be easily integrated to PICs. Different from conventional free-space-coupled or fiber-coupled SNSPDs, waveguide-integrated SNSPDs absorb light evanescently. Their optical absorption increases exponentially with the length of the superconducting nanowire. Depending on the mode overlapping, a reasonably large optical absorption can be achieved with relatively short nanowire compared to the fiber-coupled detectors (e.g., a $\sim$22-μm-long nanowire on a single mode AlN waveguide can absorb $> 95\%$ of incoming light). With a proper cavity design on the waveguide, near-perfect absorption can be achieved in nanowires with only a few micrometer length. This short length greatly enhances fabrication yield, increases detector speed, and reduces dark counts and timing jitter.

Moreover, a superconducting nanowire not only works as a photon detector, it can also work as amplifiers [38], current sensor [39], multiplexer [40], etc. In addition, the superconducting layer can be used to make electrodes for velocity-matched optical modulators [41], low-loss transmission line and antenna to deliver microwave signal to the on-chip quantum memories.

Early development of waveguide-integrated SNSPDs is mainly for the infrared wavelength region (e.g., GaAs/AlGaAs waveguide [26] and silicon-on-insulator waveguide [27]). They work for semiconductor quantum dot based single-photon sources, and spontaneously parametric down converted single photons [28, 30, 42]. Recent progress on the study of single photon sources at the visible wavelength, such as color centers in diamond, spin defects and quantum dots in wide bandgap materials, created demand on a quantum PIC that works at visible wavelength. Several waveguide materials have been pursued, including silicon nitride [29, 30], lithium niobate [37], and diamond [31, 36, 32].

Ultimately, we would like to develop a material platform that works across a broad wavelength range, from UV to IR.

Among various waveguide materials, AlN stands out as a promising, versatile candidate [43, 44]. It has an exceptionally large band gap of 6.2 eV, which offers a

broad spectral window of transparency from 200 nm to 10 μm. Its high refractive index ($n = 2.15$ at 637 nm) allows efficient optical coupling from single photon emitters in nanodiamond membranes. Its high thermal conductivity (285 W/mK) and small thermo-optic coefficient (2.32×10^{-5}/K) allow it to operate at various temperature ranges. Its intrinsic electro-optic (~1 pm/V) and piezo-electric ($d_{33} \approx 5$ pm/V) properties enable active tuning of the material/structure, and can potentially be implemented as optical modulators, which are important for feed-forward operation. Its $\chi^{(2)}$ nonlinearity (~ 4.7 pm/V) can be used for parametric frequency conversion, sum/difference frequency conversion, frequency comb generation, etc.

1.2.2 Thesis goal

The goal for this Master's thesis is to develop high-efficiency SNSPDs on AlN substrates, and integrate them with AlN photonic waveguide.

The detectors and waveguides will be designed to operate at 637 nm, which corresponds to the zero phonon line of nitrogen vacancy (NV) centers in diamond. With this design, the system will be readily available to host integrated single-photon sources in the form of diamond membranes [45]. The realization of the proposed waveguide-integrated detector will be particularly useful for the future development of a fully integrated quantum photonic processor.

1.2.3 Thesis outline

This thesis will be organized as follows:

Chapter 2 – Design and Modeling. This chapter describes the design and modeling of the waveguide-integrated detectors. We simulated the device operation using electrothermal model, and calculated the optical absorptions using a finite-difference mode solver.

Chapter 3 – Material and Fabrication. This chapter first describes the deposition and characterization of NbN thin film on AlN substrate, followed by fabrication

process of the detectors and waveguides.

Chapter 4 – Measurement and Result. This chapter describes the measurement apparatus, methods and results. The measurements include basic I-V curve, detection efficiency, and timing jitter.

Chapter 5 – Conclusion and Future Work. In this chapter, we summarize the main results of the thesis, and describes the future works.

Chapter 2

Design and Modeling

In this chapter, we present the design and modeling of the waveguide-integrated SNSPDs. To enhance detector sensitivity and signal-to-noise ratio, we adopted a parallel nanowire design. We modeled the SNSPDs using an electrothermal model, and calculated the detector absorption using a finite-difference mode solver.

2.1 Design Overview

The vision is to build a quantum PIC that has integrated single-photon emitters and detectors, as depicted in Fig 2-1. The single-photon emitters will be nitrogen vacancy (NV) centers in a diamond membrane [45], which can be transfered onto the waveguide taper. The pump light will be filtered with on-chip distributed Bragg gratings (DBGs), and the NV fluorescence will be detected using integrated SNSPDs. The waveguide material will be AlN, which is transparent at visible wavelength and has low fluorescence

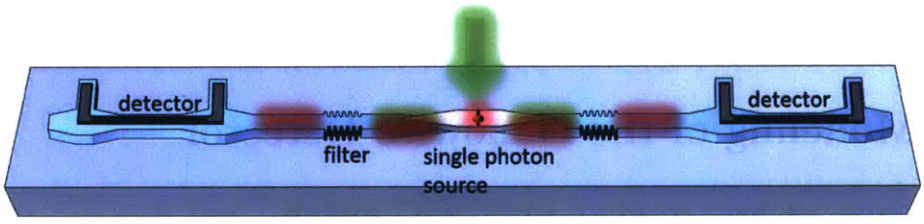

Figure 2-1: A quantum PIC with integrated single-photon source and detectors.

To enhance sensitivity and signal-to-noise ratio of the detector, we adopted a parallel nanowire architecture, known as two-element superconducting nanowire avalanche photodetector (2-SNAP) [17]. The single-nanowire width is designed to be 60 nm. Two detector lengths are used, one for 50% absorption, and one for ~100% absorption. This unique advantage of controlling absorption by changing detector length allows us to measure photon correlation without beam splitters. Figure 2-2(a) shows a possible implementation of Hanbury Brown and Twiss (HBT) measurement using waveguide-integrated detectors without beam splitters. Here, DBG 1 is to filter pump light, DBG 2 is to pass pump light while reflect signal light (single photons emitted by NV centers). The short SNSPD only absorbs 50% of light, which is similar to a 50/50 beam split, and the second SNSPD absorbs the remaining 50%. Figure 2-2(b) shows an equivalent, conventional HBT setup.

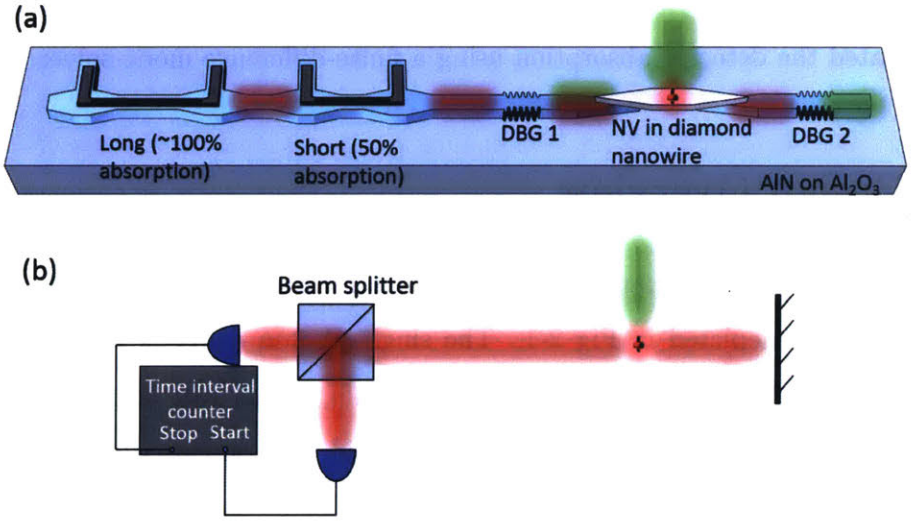

Figure 2-2: An on-chip $g^{(2)}$ measurement implemented using integrated SNSPDs without the need of beam splitters. (a) Schematics of the implementation; (b) equivalent HBT setup.

2.2 Modeling of the Nanowire Detector

In this section, we present the modeling of the SNSPDs. The detector geometry and current distribution were simulated using an electrostatic model. The device

operation was simulated using an electrothermal model. We also discussed the kinetic inductance of superconducting nanowires, and formulated the electromagnetic simulation for the transmission-line effect in SNSPDs.

2.2.1 Electrostatic simulation

Figure 2-3 shows the outline and electrostatic simulation (COMSOL Multiphysics) of the detector. The inset shows a zoomed view of the parallel nanowires. The inductor is to restrict the current from leaking during the avalanche process, and slow down the device to prevent latching. When writing the pattern using electron beam lithography, we used large beam current for the inductor and small current for the nanowire. Changing beam current usually causes pattern shift, and the overlap junction is to tolerate this misalignment.

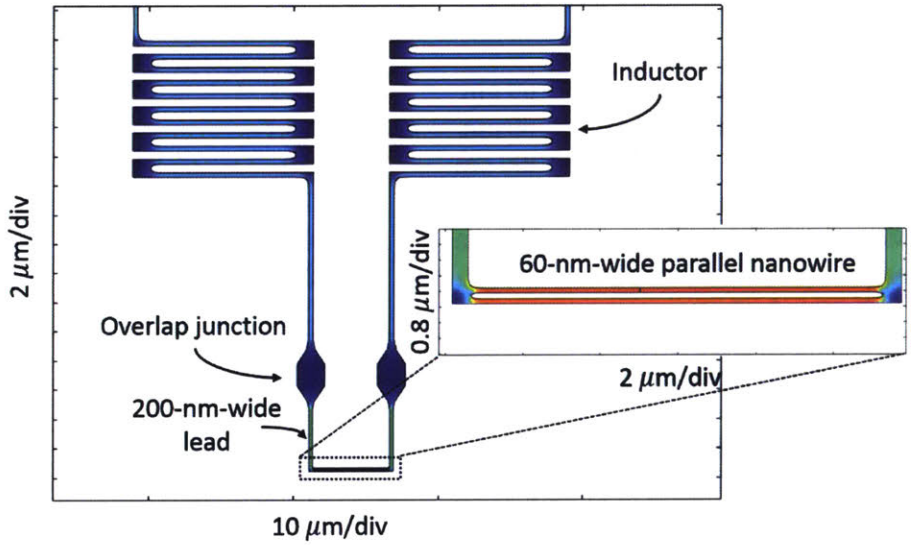

Figure 2-3: Electrostatic simulation of the 2-SNAP. The color map shows the current density distribution, which can help identify potential current crowding regions.

We import the geometry from a GDS design file, and set the material resistance to be $1\,\Omega$/sq (sq stands for square). By driving a 1 A current through the terminals, we can calculate the voltage across, and can get the number of squares of the device. [1]

[1] Number of squares is a means to describe the electrical size of a 2-D structure. For a rectangle, the number of squares equals to the ratio of the length to the width. For example, a 10 μm×1 μm rectangle will have the same resistance as a 20 μm×2 μm one, because they are both 10 sq.

The electrostatic simulation also help us to visualize the current density distribution and identify potential current crowding sites. We noticed that the upper nanowire in fact has a 1.8% higher current density than the lower one; this is because the current takes longer path (larger inductance) to travel trough the lower one. The current imbalance may limit the maximum biasing current. One way to avoid this problem is to put one of the inductor on the other side of the nanowire. This change makes the detector centrosymmetric, and ensures equal currents in the two nanowires.

Table 2.1 shows the calculated inductances for different sections of the SNAP. This breakdown list helps identify the inductance contribution from various parts, and serve as a guideline to predict the device operation.

Table 2.1: Geometry and inductance for different sections of the SNAP

Section	Width	Number of squares	Inductance (nH) (based on 94 pH/sq)
Nanowire (5 μm)[1]	60 nm	83.3	7.83
Nanowire (22 μm)[1]	60 nm	366.7	34.5
Lead[2]	200 nm	20	1.88
Overlap junction[2]	1.86 μm	7.6	0.71
Meander inductor[2]	300 nm	447.8	42.1
Other large lead to contact pads	~2 μm	217	20.4
Entire device	—	1210	113.7

[1] 5 μm is for ~50% absorption, and 22 μm is for ~97% absorption.

[2] Values are for single side only.

2.2.2 Electrothermal model

The device operation of an NbN SNSPD can be predicted by electrothermal models [46, 47, 48, 49]. This model consists of two parts: (1) the non-equilibrium thermal response in a superconducting nanowire; and (2) the electrical response of biasing/readout circuitry.

Thermal response

The thermal response after photon excitation in a superconducting thin film or nanowire can be described using a "two-temperature" model [50, 2]. Figure 2-4 shows the hot electron relaxation process. The optical excitation produces a high-energy hot electron/plasmon. The hot electrons relax through electron-electron and electron-phonon scattering. Eventually, the phonon dumps energy to the substrate, which is assumed to be a thermal bath with a constant temperature. The temperatures of the electron subsystem (T_e) and phonon subsystem (T_p) can be solved using the following equations:

$$c_\mathrm{e}\frac{\mathrm{d}T_e}{\mathrm{d}t} = -\frac{c_\mathrm{e}}{\tau_{\mathrm{e-p}}}(T_\mathrm{e} - T_\mathrm{p}) + P(t) \tag{2.1}$$

$$c_\mathrm{p}\frac{\mathrm{d}T_\mathrm{p}}{\mathrm{d}t} = \frac{c_\mathrm{e}}{\tau_{\mathrm{e-p}}}(T_\mathrm{e} - T_\mathrm{p}) - \frac{c_\mathrm{p}}{\tau_\mathrm{es}}(T_\mathrm{p} - T_\mathrm{sub}) \tag{2.2}$$

where c_e and c_p are the specific heat of electron and phonon, respectively; T_sub is the substrate temperature; $\tau_{\mathrm{e-p}}$ is the electron-phonon interaction time; τ_es is the phonon escape time; and $P(t)$ is the external perturbation. Here, electron-phonon and phonon-electron interaction time are related based on the energy balance condition $c_\mathrm{p}/\tau_{\mathrm{p-e}} = c_\mathrm{e}/\tau_{\mathrm{e-p}}$. Note that the term $\frac{c_\mathrm{p}}{\tau_\mathrm{es}}(T_\mathrm{p}-T_\mathrm{sub})$ describes the phonon escape to the substrate. It can be modeled using a more general thermal boundary conductance, or a Kapitza resistance. The thermal transport over the boundary follows $\frac{\mathrm{d}}{\mathrm{d}t}Q = \sigma(T_\mathrm{p}^\eta - T_\mathrm{sub}^\eta)$, where η is usually 4, and can range from 3 to 6, depending on the type of boundary.

In a current-carrying superconducting nanowire (assuming 1-D), considering Joule heating and thermal diffusion, the two-temperature model can be written in the following partial differential equations (PDEs) [47]:

$$\frac{\partial c_\mathrm{e}(T_\mathrm{e})T_\mathrm{e}}{\partial t} = -\frac{c_\mathrm{e}(T_\mathrm{e})}{\tau_{\mathrm{e-p}}(T_\mathrm{e})}(T_\mathrm{e} - T_\mathrm{p}) + J^2\rho + \frac{\partial}{\partial x}[\kappa_\mathrm{e}(T_\mathrm{e})\frac{\partial T_\mathrm{e}}{\partial x}] \tag{2.3}$$

$$\frac{\partial c_\mathrm{p}(T_\mathrm{p})T_\mathrm{p}}{\partial t} = \frac{c_\mathrm{e}(T_\mathrm{e})}{\tau_{\mathrm{e-p}}(T_\mathrm{e})}(T_\mathrm{e} - T_\mathrm{p}) - \frac{c_\mathrm{p}(T_\mathrm{p})}{\tau_\mathrm{esc}}(T_\mathrm{p} - T_\mathrm{sub}) + \frac{\partial}{\partial x}[\kappa_\mathrm{p}(T_\mathrm{p})\frac{\partial T_\mathrm{p}}{\partial x}] \tag{2.4}$$

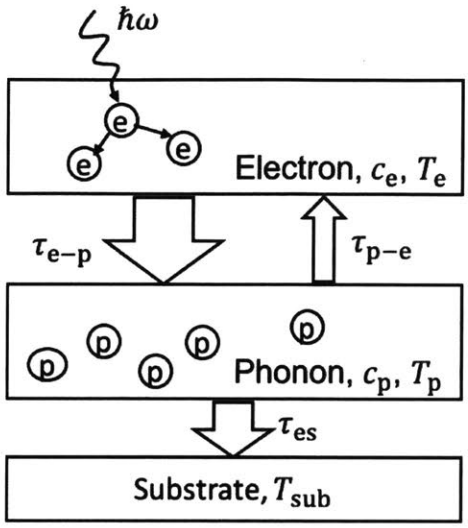

Figure 2-4: Hot electron relaxation and thermalization process in two-temperature model. Adapted from Ref. [2]

where J is the current density, ρ is the resistivity, $\kappa_{\mathrm{e,p}}$ is the diffusion coefficient for electron and phonon. Without loss of generality, $c_{\mathrm{e,p}}$, $\tau_{\mathrm{e-p}}$, and $\kappa_{\mathrm{e,p}}$ are temperature dependent.

In the literature, instead of the general form of the two-temperature model, a simplified bolometric description is usually used [47, 46]. It uses a reduced temperature (T_{r}) by approximating phonon and electron with the same temperature. The approximation is reasonable given that $\tau_{\mathrm{p-e}}$ and τ_{esc} (e.g., on Sapphire) are on the same order, so the electron and phonon systems are approximately at equilibrium. The bolometric equation can be derived by adding Eq. 2.3 and 2.4:

$$\frac{\partial}{\partial t}[c(T_{\mathrm{r}})T_{\mathrm{r}}] = J^2\rho - \frac{c_{\mathrm{p}}(T_{\mathrm{r}})}{\tau_{\mathrm{esc}}}(T_{\mathrm{r}} - T_{\mathrm{sub}}) + \frac{\partial}{\partial x}[\kappa(T_{\mathrm{r}})\frac{\partial T_{\mathrm{r}}}{\partial x}] \tag{2.5}$$

where $c(T_{\mathrm{r}}) = c_{\mathrm{p}}(T_{\mathrm{r}}) + c_{\mathrm{e}}(T_{\mathrm{r}})$, $\kappa(T) = \kappa_{\mathrm{e}}(T_{\mathrm{r}}) + \kappa_{\mathrm{p}}(T_{\mathrm{r}})$.

If we further neglect the phonon diffusion, and the spatial variation of κ_{e}, we will reach the heat equation used in [46]:

$$\frac{\partial}{\partial t}[c(T_{\mathrm{r}})T_{\mathrm{r}}] = J^2\rho - \frac{\alpha}{d}(T_{\mathrm{r}} - T_{\mathrm{sub}}) + \kappa_{\mathrm{e}}(T_{\mathrm{r}})\frac{\partial^2 T_{\mathrm{r}}}{\partial x^2} \tag{2.6}$$

where we have replaced phonon-substrate coupling coefficient to α/d. $\alpha = AT_{\mathrm{r}}^3$ is

the heat-transfer coefficient per unit area, or thermal boundary conductance; and d is the film thickness.

Electrical circuit response

Figure 2-5(a) shows the equivalent circuit for a conventional SNSPD, and Fig. 2-5(b) shows the equivalent circuit for the 2-SNAP used in our waveguide integration. L_{k1} and L_{k2} are the kinetic inductances of the 60-nm-wide parallel nanowires. Since the hotspot size is small compared to the length of the nanowire, we assumed the kinetic inductance of the nanowire to be constant. L_s represents the series inductance made of 300-nm-wide superconducting meander wires; R_{n1} and R_{n2} are state-dependent variable resistances, whose values need to be determined from the thermal model. The load impedance R_{load} is $50\,\Omega$. The voltage appears across R_{load} is the output signal (before amplification).

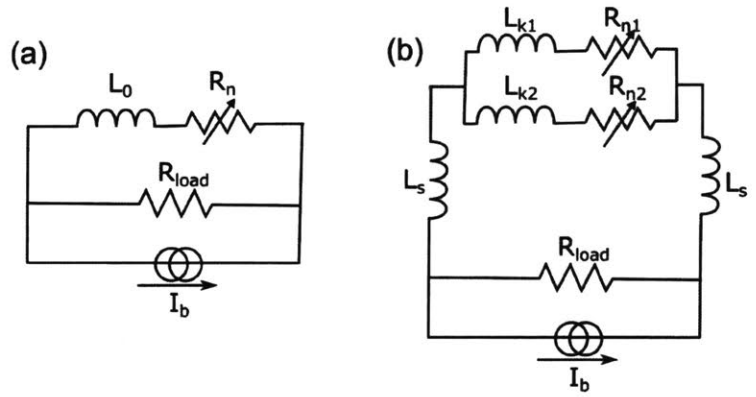

Figure 2-5: Equivalent circuit for a conventional SNSPD (a) and a 2-SNAP used in our waveguide integration (b).

The 2-SNAP circuit can be described by two ordinary differential equations (ODEs) with dependent variables I_1 and I_2:

$$2L_s(\frac{\mathrm{d}}{\mathrm{d}t}I_1 + \frac{\mathrm{d}}{\mathrm{d}t}I_2) + L_{k1}\frac{\mathrm{d}}{\mathrm{d}t}I_1 + R_{n1}I_1 = (I_b - I_1 - I_2)R_{load} \tag{2.7}$$

$$L_{k1}\frac{\mathrm{d}}{\mathrm{d}t}I_1 + R_{n1}I_1 = L_{k2}\frac{\mathrm{d}}{\mathrm{d}t}I_2 + R_{n2}I_2 \tag{2.8}$$

where I_1 and I_2 are the currents in the two parallel nanowires. The values of R_{n1} and R_{n2} can be calculated as

$$\int_{J(x)>J_c(T(x))} \frac{\rho_n}{dw} \mathrm{d}x \tag{2.9}$$

where x is the position on the nanowire, d is the film thickness, w is the nanowire width, ρ_n is the resistivity at normal state, $J(x)$ is the current density in the nanowire, and $J_c(T(x))$ is the local temperature-dependent critical current density.

Determining the fitting parameters

The bolometric formula greatly reduces the number of fitting parameters needed. Table 2.2 lists the material parameters for our NbN film on AlN-on-sapphire substrate used for device fabrication.

ξ, c_e, and c_p are adopted from [51]. T_C and R_s were measured on freshly deposited films (see Section 3.1.3 for details). d was measured using an atomic force microscope (AFM). Based on the measured sheet resistance and film thickness, the room-temperature resistivity is $\sim 2.5\,\mu\Omega$-m, which is consistent but slightly higher than that reported in [51]. We noticed that the room-temperature sheet resistance increased to $\sim 600\,\Omega/\mathrm{sq}$ after device fabrication, which is likely due to oxidation.[2] The kinetic inductance was fitted from the falling edge of the detector pulse. London penetration depth was calculated from $L'_K = \mu_0\lambda^2$, where L'_K is the kinetic inductivity. Our estimation is consistent with that reported in [52].

The thermal boundary conductance coefficient, A, was determined by fitting the retrapping current, and the details will be discussed in Section 4.2. We found that the formula given in [53] was not able to give us a reasonable α for the one-temperature model [47]. Instead, we used a value that matches the simulated retrapping current to the measured one.

The diffusion coefficient, κ, can be calculated using the Wiedemann-Franz law

[2]The "sheet reistance after fabrication" was estimated by measure the total resistance of the fabricated device divided by the number of squares of the device calculated from COMSOL simulation. The sheet kinetic inductivity was also estimated by dividing the total kinetic inductance of the device by the number of calculated squares.

($\kappa = LT/\rho$, where $L = 2.45 \times 10^{-8}\mathrm{W\Omega/K^2}$ is the Lorenz number) for normal state, and $\kappa_s/\kappa_n = T/T_C$ for superconducting state [46].

Table 2.2: Material parameters for NbN thin films used in device fabrication

Parameter	Description	Value
T_C	Critical temperature	11 K
$\Delta(0)$	Gap energy	2 meV
d	Film thickness	4.8 nm
$\xi(0)$	Ginzburg-Landau coherent length	7.5 nm [51]
$\lambda(0)$	Thin-film London penetration depth	528 nm
R_s	Room-temperature sheet resistance	530 Ω/sq (fresh film) 600 Ω/sq (after fabrication)
L_s	Sheet kinetic inductance @ 2.5 K	94 pH/sq
c_e	Electron specific heat (at 10 K)	2.4 mJ $\mathrm{cm^{-3}K^{-1}}$ [51]
c_p	Phonon specific heat (at 10 K)	9.8 mJ $\mathrm{cm^{-3}K^{-1}}$ [51]
A	Thermal boundary conductance coefficient	400 $\mathrm{W/m^2K}$
$J_c(0)$	Critical current density	0.03 $\mu\mathrm{A/nm^2}$

Here, the temperature dependence of the parameters follows that in [51]:

$$\xi(T) = \xi(0)(1 - T/T_C)^{-1/2} \tag{2.10}$$

$$\Delta(T) = 2.15 k_B T_C[1 - (T/T_C)^2] \tag{2.11}$$

$$\lambda(T) = \lambda(0)(1 - T/T_C)^{-1/2} \tag{2.12}$$

$$J_c(T) = J_c(0)(1 - (T/T_C)^2)^{3/2}(1 + (T/Tc)^2)^{1/2} \tag{2.13}$$

For comparison, Table 2.3 lists the parameters for bulk NbN [54].

Table 2.3: Material parameters for bulk NbN

Parameter	Description	Value
T_C	Critical temperature	16 K
$\xi(0)$	Ginzburg-Landau coherent length	5 nm
$\lambda(0)$	London penetration depth	200 nm
$\Delta(0)$	Energy gap	2.4 meV
$H_{c2,0}$	Upper critical field	15 T

Model implementation

We implemented the electrothermal model in COMSOL Multiphysics. We build the model to be one-dimensional based on two reasons: (1) the width (w) and thickness (d) of the nanowire are $\ll \lambda$, so the current distribution can be assumed uniform on the cross section; (2) though $w > \xi$, the temperature profile along the width is not important for the calculation of hotspot dynamics and electrical output.

Figure 2-6 depicts how we set up the model.

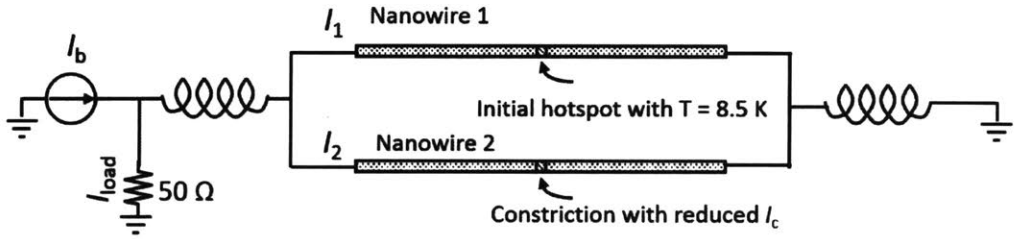

Figure 2-6: Schematic of the simulated 2-SNAP. A ξ-long section in the middle of Nanowire 1 was set to be 8.5 K at t = 0 to simulate the initial hotspot from photon excitation. A ξ-long section in the middle of Nanowire 2 was assigned to have $0.99\,I_C$ to simulate a constriction, so that the switching will happen deterministically.

Two PDE solvers (Eq. 2.6) were used to calculate the time-dependent temperature profiles T_1 and T_2 in Nanowire 1 and Nanowire 2, respectively. The initial condition were set to be 2.45 K, which is the base temperature of our cryogenic probe station. To simulate the photon excitation, we set a ξ-long section in the middle of Nanowire 1 to be at 8.5 K at time 0. Also, we made a ξ-long section in the middle of Nanowire 2 to have $0.99I_c$, which essentially simulates a small constriction that allows the switching to happen deterministically when bias current exceeds critical current.

One ODE solver was used to model the circuit response (Eq. 2.7 and 2.8) and calculate the currents I_1 and I_2. The initial conditions for I_1 and I_2 are both set to be $0.5I_b$. In the case where L_{k1} and L_{k2} are not equal, the initial current will be distributed according to the inductances.

Simulating the 2-SNAP operation

Figure 2-7 shows the simulated hotspot dynamics, and Fig. 2-8 shows the time-evolution of the current distribution and resistance change. At time 0, the initial hotspot appears at the center of Nanowire 1. Because of the resistive heating, the hotspot expands, and pushes the current to Nanowire 2. At the avalanche point, where I_2 exceeds the critical current in Nanowire 2, the constriction switches and a hotspot starts to grow. As R_{n1} and R_{n2} grow, bias current is diverted to the load, and the hotspot starts to cool. When the nanowires become superconducting again, bias current flows back to the nanowires with a time constant of $\tau \sim L/R$, where R is the load resistance, and L is the total inductance of the detector. In the simulation, we set the bias current to $95\%I_C$.

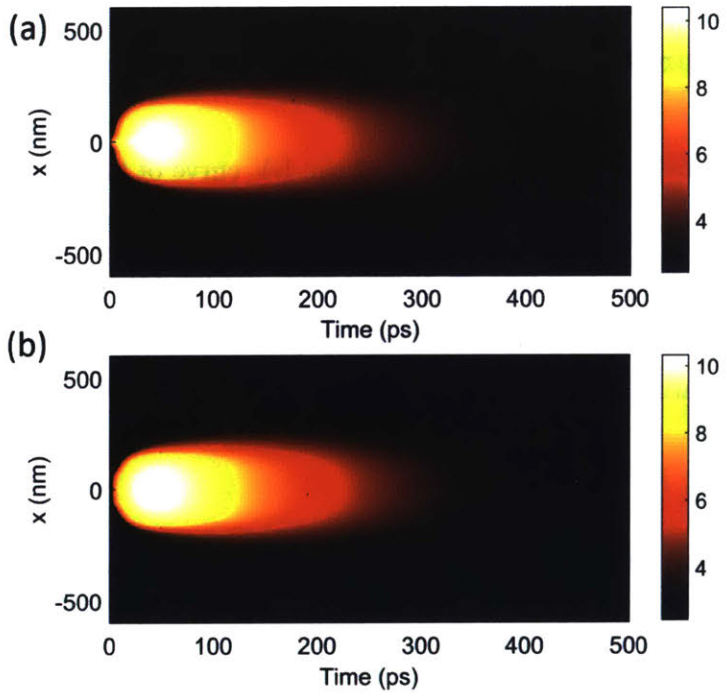

Figure 2-7: Electrothermal simulation of the hotspot dynamics in a 2-SNAP.

Simulating the retrapping current

To simulate the retrapping current, we treat the 60-nm-wide parallel nanowires to be a single 120-nm-wide wire, and put a ξ-long constriction with $0.99I_{SW}$ at the center.

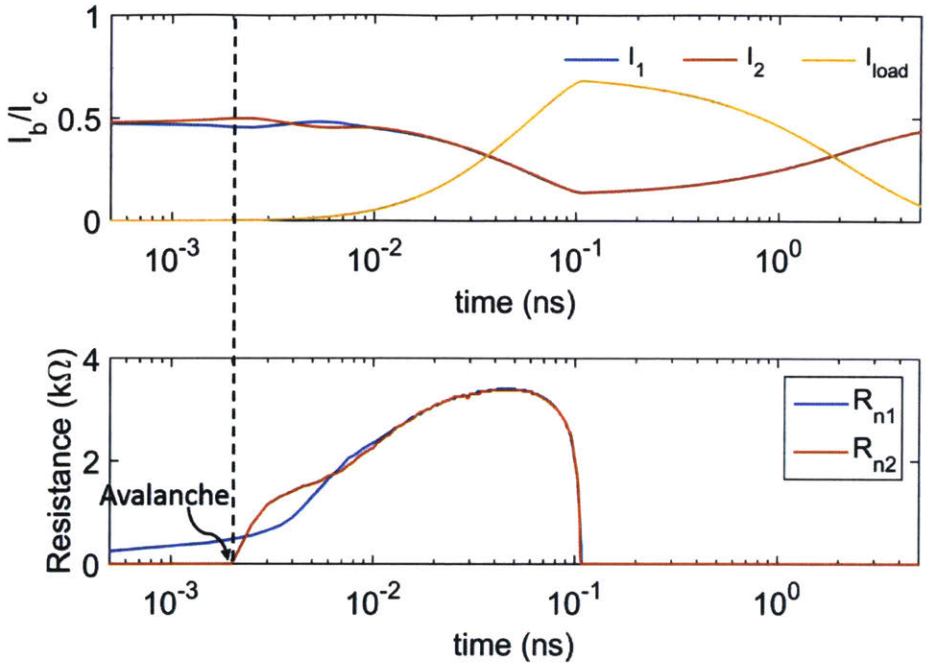

Figure 2-8: Electrothermal simulation of the current and resistance of a 2-SNAP.

By sweeping the bias current, we simulated the I-V curve of the nanowire. Figure 2-9(a) shows the equivalent circuit for the simulation. Figure 2-9(b) shows the input bias current. The ramp rate was set to be 1 kHz. Figure 2-9(c) shows the simulated I-V curve, in which the retrapping current matches our measurement in Section 4.2. The base temperature was set to 3.8 K, and the nanowire length was 5 μm.

2.2.3 Kinetic inductance in normal metals and superconductors

Kinetic inductance plays a key role in superconducting nanodevices. The physical origin of kinetic inductance is the inertia of charge carriers (e.g., electrons or Cooper pairs). When driving metals/superconductors with an oscillating electric field, part of the energy is stored as the kinetic energy of the charge carriers. This effect exists in both normal metals and superconductors. Here, we compare the kinetic inductances of normal metals and superconductors.

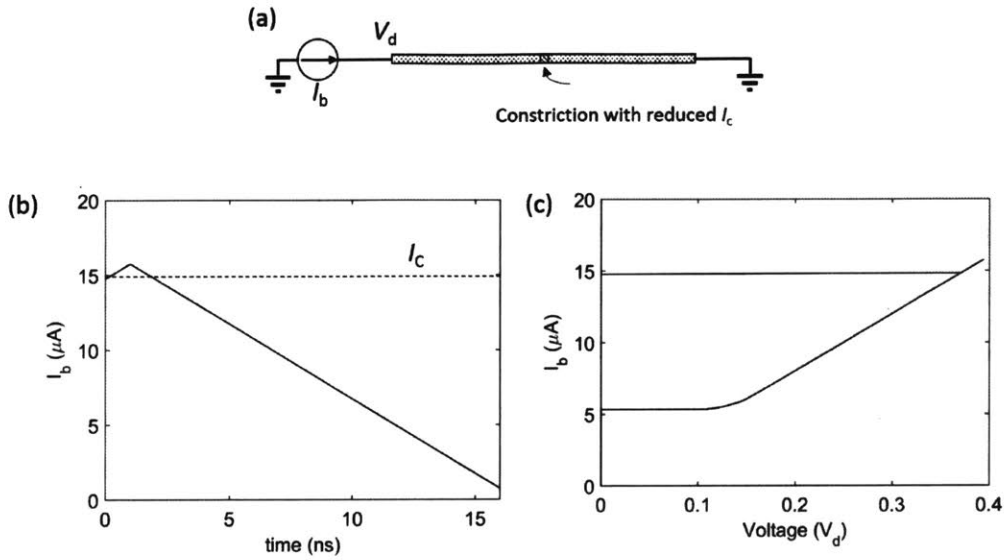

Figure 2-9: Electrothermal simulation of retrapping current.

Normal metals. For normal metals, it is intuitive to analyze using the Drude model. We start with a free-electron sea under an oscillating electric field E,

$$\frac{p}{\tau} + \frac{\mathrm{d}p}{\mathrm{d}t} = -eE \tag{2.14}$$

where $p = mv$ is the momentum of electron, $1/\tau$ is the scattering rate. We substitute in the current density $J = -nev$ (n is the free electron density), and transform the equation to frequency domain:

$$J = \frac{ne^2/m}{1/\tau - i\omega} E = \sigma(\omega) E \tag{2.15}$$

where $\sigma(\omega)$ is the frequency-dependent complex conductivity. Its inverse gives the complex impedance:

$$\rho(\omega) = 1/\sigma(\omega) = \frac{1}{\tau}\frac{m}{ne^2} - i\omega\frac{m}{ne^2} = R' - i\omega L'_{\mathrm{K}} \tag{2.16}$$

That is, for normal metal, the kinetic inductivity is

$$L'_{\mathrm{K}} = \frac{m}{ne^2} \tag{2.17}$$

The energy stored in this inductance is $\frac{1}{2}L_{\mathrm{K}}J^2 = \frac{1}{2}\frac{m}{ne^2}(-nev)^2 = \frac{1}{2}mv^2n$, which is precisely the kinetic energy of electrons.

Let's substitute in some real values. For Au, $n = 5.9 \times 10^{28}$ m^{-3}, $\omega_{\mathrm{P}} = 2\pi \times 2.18\,\mathrm{PHz}$, which is in the UV, and $1/\tau \approx 17$ THz [55].[3] Based on Eq.(2.16), its kinetic inductivity, L'_{K}, is 6×10^{-22} H-m, and resistivity is $10^{-8}\,\Omega$-m. For the kinetic inductance to become nontrivial compared to the ohmic loss, the excitation frequency has to be close to the scattering rate, i.e., THz regime.

Assuming all the bulk parameters hold at the nanometer scale, a 4-nm-thick, 100-nm-wide, 45-μm-long Au nanowire would have a kinetic inductance of only 67.5 pH, while a resistance of 1.1 kΩ. At 10 GHz, for example, the corresponding reactance is 4.24 Ω, which is more than 2 orders of magnitude smaller than the ohmic resistance.

At optical frequencies, however, the kinetic inductance of Au starts play a critical role; and the ratio between the energies stored in the kinetic inductance (moving electrons) and Faraday inductance (magnetic field) can be used to define the boundary between metal optics and plasmonics [56, 57].

Superconductors. In superconductors, the kinetic inductance also originates from the inertia of charge carriers, which are primarily the Cooper pairs. At frequencies much less than gap energy $f = \omega/2\pi = 2\Delta/h \approx 1.76k_BT_C/h \approx 73\,\mathrm{GHz}\times T_{\mathrm{C}}$, the complex conductivity, $\sigma(\omega) = \sigma_1(\omega) - i\sigma_2(\omega)$, of superconductors is related to the normal-state conductivity, σ_n, by the Mattis-Bardeen equation [58, 59],

$$\frac{\sigma_1(\omega)}{\sigma_n} = \frac{2}{\hbar\omega}\int_{\Delta}^{\infty} \frac{E^2 + \Delta^2 + \hbar\omega E}{\sqrt{E^2 - \Delta^2}\sqrt{(E+\hbar\omega)^2 - \Delta^2}}[f(E) - f(E+\hbar\omega)]\mathrm{d}E \qquad (2.18)$$

$$\frac{\sigma_2(\omega)}{\sigma_n} = \frac{1}{\hbar\omega}\int_{\Delta}^{\Delta+\omega} \frac{E^2 + \Delta^2 - \hbar\omega E}{\sqrt{E^2 - \Delta^2}\sqrt{\Delta^2 - (E-\hbar\omega)^2}}[1 - 2f(E)]\mathrm{d}E \qquad (2.19)$$

[3] In the Drude model, $\omega_{\mathrm{P}} = \sqrt{\frac{ne^2}{m\epsilon_0}}$ is called plasma frequency, above which the metal becomes "semi-transparent."

where $f(E)$ is the distribution function of the quasiparticles (unpaired electrons), and in thermal equilibrium, it follows the Fermi-Dirac distribution $f(E) = 1/(e^{E/k_BT}+1)$.

When $T \to 0$ and $\hbar\omega \ll \Delta$, $\sigma_1(\omega)$ vanishes, and $\sigma_2(\omega) \approx \frac{\pi\Delta\sigma_n}{\hbar\omega}$. This leads to a kinetic inductivity of

$$L'_{\mathrm{K}} = \frac{1}{\omega\sigma_2(\omega)} \approx \frac{\hbar}{\pi\Delta}\rho \tag{2.20}$$

where $\rho = 1/\sigma_n$ is the normal-state resistivity.

If we follow the BCS relation $\Delta = 1.76k_BT_C$, $L'_{\mathrm{K}} \approx 1.38\rho/T_C$ [pH-m]; or $\Delta = 2.15k_BT_C$, $L'_{\mathrm{K}} \approx 1.78\rho/T_C$ [pH-m] based on [51]. This formula is very useful because once we know the resistance and T_{C} of an SNSPD, we can estimate its kinetic inductance.

For a 4-nm-thick NbN film with a sheet resistance of 500 Ω/sq and T_{C} of 10 K, the kinetic inductivity is 3.56×10^{-19} H-m, which is 593 times of that in Au (based on the Drude analysis in the previous section). A 4-nm-thick, 100-nm-wide, 45-μm-long nanowire made from such NbN film will have an inductance of 31 nH (corresponding to an reactive impedance of 1.95 kΩ at 10 GHz); and at the same time, its resistance is zero when $T \to 0$.

2.2.4 Transmission-line effect in SNSPDs

Recently, we identified that transmission-line effect is non-negligible in SNSPDs [21, 20]. A careful engineering of this effect in SNSPDs can help improve device performance and add new functionality to the existing device architecture. To understand and model the transmission-line effect, we need to perform accurate electromagnetic (EM) simulations. In this section, we describe how to model superconducting materials for EM simulations.

The treatment of superconductor at microwave frequency is very similar to that of metal at optical frequencies. We try to simplify the EM description of a superconductor into a single frequency-dependent permittivity, which can be readily used in commercial software, e.g., COMSOL, Lumerical FDTD, etc.

From the Ampere's law we have

$$\nabla \times \mathbf{H} = -i\omega\epsilon\mathbf{E} + \mathbf{J} \tag{2.21}$$

Based on the two-fluid model, the current in superconductor consists of two parts [60]:

$$\mathbf{J} = \mathbf{J}_{\mathrm{n}} + \mathbf{J}_{\mathrm{s}} \tag{2.22}$$

$\mathbf{J}_{\mathrm{n}}$ is normal electron, which follows

$$\mathbf{J}_{\mathrm{n}} = \sigma_{\mathrm{n}}\mathbf{E}$$

where σ_{n} is the normal electron conductivity. Using the Drude model, we can estimate σ_n as $\sigma_n = \frac{ne^2/m}{1/\tau - i\omega}$, where n is the normal electron density, m is the electron mass, and $1/\tau$ is the damping rate.

$\mathbf{J}_{\mathrm{s}}$ is the super current, which follows the London equation

$$\mathbf{E} = -i\omega\Lambda\mathbf{J}_{\mathrm{s}} \tag{2.23}$$

where $\Lambda = \mu_0\lambda^2$, and λ is the penetration depth.

Inserting the expression for the current terms to the Ampere's law and assuming $\epsilon = \epsilon_0$ for superconductor,[4] we can rewrite the Ampere's law into the "source-free" form

$$\nabla \times \mathbf{H} = -i\omega\epsilon_0(1 - \frac{1}{\omega^2\mu_0\lambda^2\epsilon_0} + \frac{i\sigma_{\mathrm{n}}}{\omega\epsilon_0})\mathbf{E} \tag{2.24}$$

Here, we have formulated the relative permittivity, ϵ_r, for superconductor, and it takes the form $\epsilon_r = 1 - 1/(\omega^2\mu_0\lambda^2\epsilon_0) + i\sigma_{\mathrm{n}}/(\omega\epsilon_0)$.

With this formulation, the EM behavior of superconductors can be calculated using the following "source-free" Maxwell's equations, and the superconducting waveguides can be simulated with standard EM solvers.

[4]This assumption is just for simplicity. In reality, ϵ here refers to $\epsilon_0\epsilon_\infty$.

$$\nabla \cdot \mathbf{D} = 0 \tag{2.25}$$

$$\nabla \cdot \mathbf{B} = 0 \tag{2.26}$$

$$\nabla \times \mathbf{E} = i\omega\mu_0\mathbf{H} \tag{2.27}$$

$$\nabla \times \mathbf{H} = -i\omega\epsilon_0\epsilon_r\mathbf{E} \tag{2.28}$$

with $\mathbf{D} = \epsilon_0\epsilon_r\mathbf{E}$, $\mathbf{B} = \mu_0\mathbf{H}$, and $\epsilon_r = 1 - 1/(\omega^2\mu_0\lambda^2\epsilon_0) + i\sigma_n/(\omega\epsilon_0)$; or $\epsilon_r = 1 - 1/(\omega^2 L'_k\epsilon_0) + i\sigma_n/(\omega\epsilon_0)$, where $L'_K = \mu_0\lambda^2$ is the kinetic inductivity.

2.3 Optical Simulations

In this Section, we simulated the waveguide modes and optical absorption of the detectors using a commercial finite-difference mode solver (Lumerical Mode Solutions).

2.3.1 Waveguide mode

The AlN waveguide was designed to be a single-mode ridge waveguide that supports only the fundamental TE and TM modes.[5] The design wavelength was 637 nm, which corresponds to the zero-phonon line of NV centers.

Figure 2-10 shows the schematic of the simulated waveguide structure. The waveguide thickness was 200 nm, which was restricted by limited choices of commercially available AlN-on-sapphire substrates. The waveguide width has the following constraints. First, it has to be chosen so that it only supports the fundamental TE and TM modes. Secondly, it needs to be small for better field confinement and higher detector absorption, but reasonably wide so that the SNSPDs can be aligned with some tolerance.

[5]Pure TE or TM modes does not exist in rectangular dielectric waveguides. Here, "TE" mode refers to the mode in which H_x and E_y dominate. This mode is usually called an HE_{00}, E^y_{11}, or "TE-like" mode. Similarly, the "TM" mode here refers to the mode in which H_y and E_x dominate. This mode is usually called an EH_{00}, E^x_{11}, or "TM-like" mode. In our waveguide design, the width-to-height raio was designed to be larger than 2. As a result, the "TE-like" and "TM-like" modes are very distinguishable. Therefore, I will simply use "TE" and "TM" modes.

Figure 2-11 shows the effective index (n_{eff}) of the guided mode as a function of waveguide width. In the simulation, the refractive indices of AlN and sapphire were taken to be 2.1493 and 1.7657 respectively. As we can see, the cut-off width for the waveguide to support a guided mode is 340 nm. And for width larger than 740 nm, higher order modes start to appear.

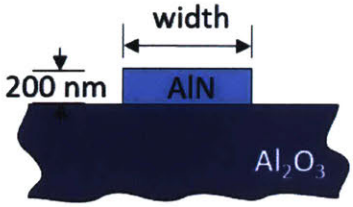

Figure 2-10: Schematic of the simulated waveguide structure.

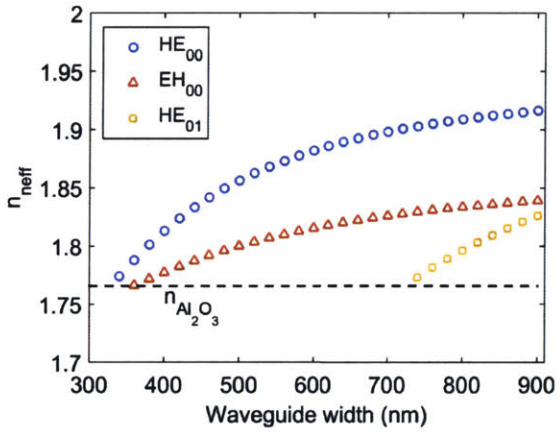

Figure 2-11: Simulation of the waveguide modes with different waveguide widths.

Considering all above-mentioned factors, we chose the width to be 450 nm. Figure 2-12 shows the mode pattern ($|E|^2$) of the fundamental TE and TM modes of the waveguide. The effective indices of the two modes are 1.84 and 1.79, respectively.

2.3.2 Detector absorption on waveguide

A traveling-wave detector absorbs light evanescently, and its absorption rate can be estimated from the imaginary part of n_{eff} of the waveguide mode with integrated superconducting nanowires. The relation between absorption rate α and n_{eff} can be identified from the following equation:

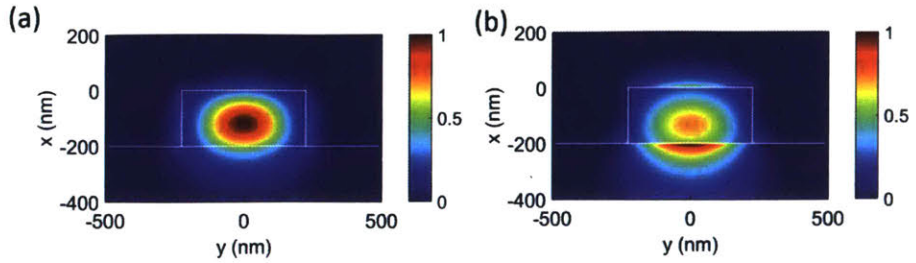

Figure 2-12: Mode patterns ($|E|^2$) of the fundamental TE (a) and TM (b) modes in a 450-nm-wide waveguide at 637 nm.

$$P(z) \propto \iint |E_0(x,y)e^{in_{\text{eff}}k_0 z}|^2 \mathrm{d}x\mathrm{d}y = \iint |E_0(x,y)|^2 \mathrm{d}x\mathrm{d}y e^{-k_0 2n''_{\text{eff}} z} = \iint |E_0(x,y)|^2 \mathrm{d}x\mathrm{d}y e^{-\alpha z} \tag{2.29}$$

where $P(z)$ is the power on the cross section of the waveguide, $E_0(x,y)$ is the electric field of the guided mode, k_0 is the free-space wave vector, $n_{\text{eff}} = n'_{\text{eff}} + in''_{\text{eff}}$ is the complex effective index, and α is the propagation loss rate. In our simulated structure, the dielectric materials are assumed to be lossless, and the only loss channel is the superconducting material (NbN).

The active region (i.e., the absorbing region) of the SNSPD consists of two 60-nm-wide, 5-nm-thick parallel NbN nanowires with a 80 nm gap. We add this absorbing element to the simulation (see Fig. 2-13), and calculated the effective indices to be $1.8368 + i0.0089$ and $1.7863 + i0.0078$ for TE and TM modes respectively, corresponding to an absorption rate of 0.762 dB/μm and 0.667 dB/μm. Because the NbN film is only 5 nm thick, it barely perturbs the mode.

The mesh size in the nanowire region and its close proximity was set to be 0.5 nm in the vertical direction and 1 nm in the horizontal direction. The complex relative premittivity of NbN was set to be $-7.23 + i17.03$ [61].

A practical issue in fabrication is the misalignment between waveguides and NbN nanowires. To study the effect of misalignment on the absorption rate, we calculated the absorption rate as a function of position shift of NbN nanowires from

the center. Figure 2-13(a) shows the schematic of the simulated structure, and (b) shows the result. At a misalignment of 50 nm, which is very common in practice, the absorption rate drops from 0.7617 μm/dB and 0.6671 μm/dB to 0.7099 μm/dB and 0.6317 μm/dB for TE and TM mode respectively, i.e., a reduction of 6.8% and 5.3%. This effect is not detrimental. For example, a 97% designed absorption will drop to ~91%. To compensate this effect, we may increase the length of the detector by ~6%. In fact, other practical issues, e.g., waveguide loss, scattering loss on the detector site, may contribute even more than the misalignment.

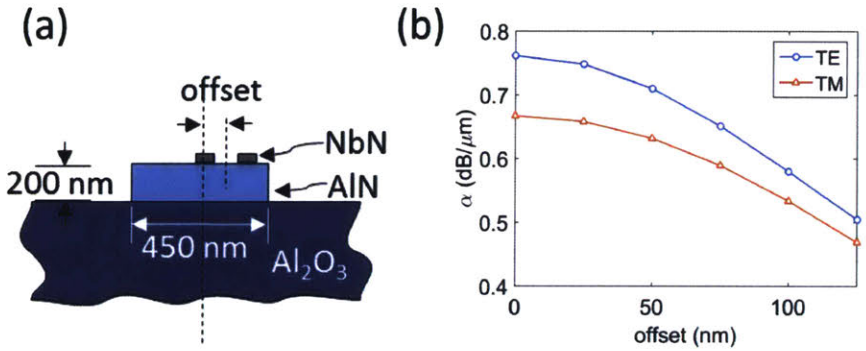

Figure 2-13: The effect of misalignment on absorption rate. (a) Schematics of the simulated structure. (b) Absorption rate as a function of misalignment for TE and TM modes.

Chapter 3

Material and Fabrication

In this chapter, the material deposition and device fabrication processes are described. Figure 3-1 shows the process overview. The detectors were made of ~5-nm-thick NbN films, and the waveguides were made from 200-nm-thick AlN films on sapphire substrate. Three lithography steps were involved: one photolithography step to define gold electrical contact pads and alignment marks, and two aligned electron-beam lithography (EBL) steps to define nanowires and waveguides. Besides detailed process and parameters, the challenges and common problems are also discussed.

3.1 Superconducting Thin Film Deposition

The performance of an SNSPD is critically affected by the quality of the superconducting thin film. At the few-nanometer length scale, the electrical and optical properties of the film become extremely sensitive to material composition, crystal phase, disorders, inhomogeneities, contaminants, film thickness, and substrate material; and many of these factors can be controlled through the deposition process. In this section, we describe the deposition and characterizations of NbN thin films on AlN-on-sapphire substrates.

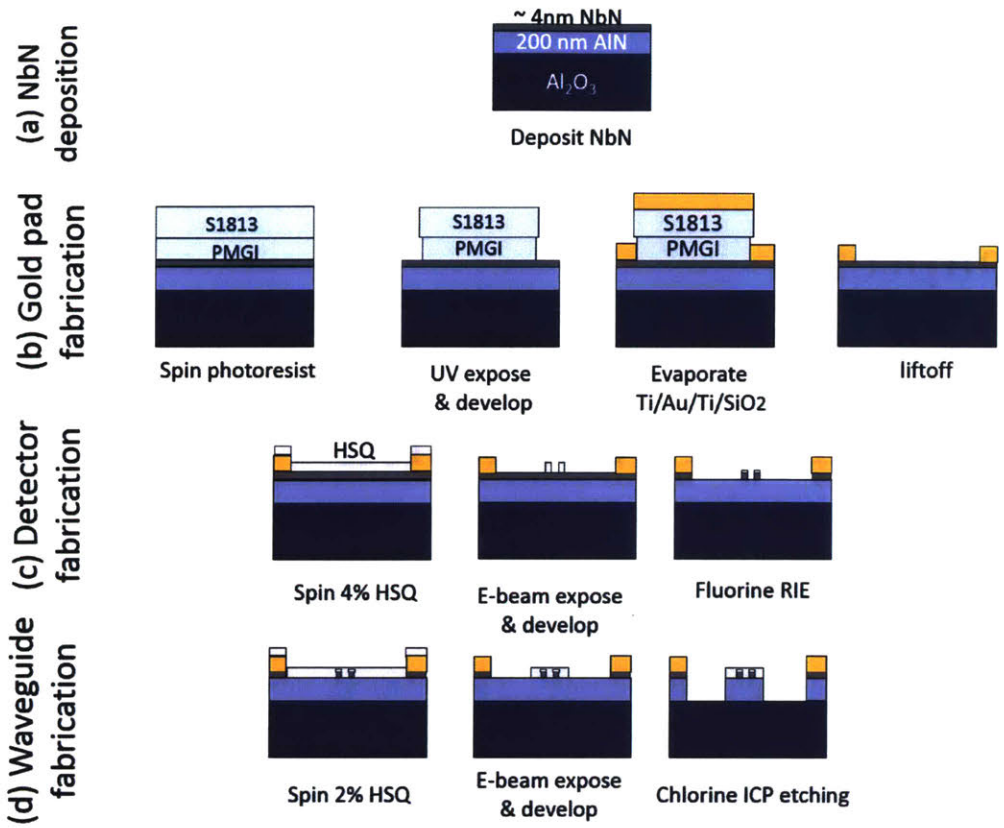

Figure 3-1: Overview of the fabrication process flow.

3.1.1 Substrate preparation

The AlN-on-sapphire wafers were purchased from Kyma Thechonologies. The AlN film is c-axis oriented single crystal with a thickness of 200 nm ($\pm$10%). The substrate comes as 2- or 4-inch wafers. To dice the wafer to small pieces, we first coated it with photoresist (spin S1813 at 3 krpm for 1 min, bake at 90 °C for 3 min), then cut it into 1 cm$\times$1 cm pieces using a dicing saw (Disco DAD3240). Dicing sapphire is hard. To break fewer blades, we slowed down the spindle speed (2 krpm) and moving speed (0.5 mm/s); and instead of cutting all the way down at once, we made 2 cuts for each line, where each cut only cut half of the intended depth.

Before deposition, the substrate pieces were sonicated in acetone for 3 min, and rinsed with methanol and IPA. Then, they were cleaned using a oxygen plasma asher at 100 W for 3 min. The oxygen plasma ashing completely removes the photoresist

coating, and activates the substrate surface.

3.1.2 Deposition process

The NbN films were deposited using reactive DC magnetron sputtering in an AJA sputtering system.

The sputtering process was based on Andrew Dane's recipe as reported in [35]. There are six major steps:

1. Heat the substrate holder to a nominal temperature of 840 °C, and soak for 20 min. The elevated temperature gives the deposited atoms enough energy to rearrange and form a stress-free crystal lattice.

2. Flow Ar gas at 26.5 sccm at 30 mTorr, and ignite the plasma. This high pressure is to allow enough gas in the camber for easy plasma ignition. The chamber pressure is controlled through the gate valve between the cryopump and the main chamber. The DC current is set to be 400 mA.

3. Keep the Ar flow rate at 26.5 sccm and reduce chamber pressure to 2.5 mTorr.

4. Flow Ar:N_2 gas at 26.5 sccm:8 sccm. The pressure holds at 2.5 mTorr, and DC current holds at 400 mA. Keep the condition for 3 min.

5. Open the shutter and start the deposition.

6. Close the shutter and cool the substrate holder.

The base pressure of the chamber before the process starts is normally ~6.8e-9 Torr. After a 20 min heat soak, the chamber pressure usually increases to ~1.8e-8 Torr. These values are useful indicators of the system, and help us identify possible contamination in the chamber. They are monitored for every deposition.

To get 4-5 nm NbN film, the deposition time was around 76 s. However, the deposition rate changes over time. We perform routine depositions to monitor it, and adjust the deposition time to get the desired films for devices.

3.1.3 Characterization

Every film was characterized after deposition. The routine characterizations include room-temperature sheet resistance, superconducting critical temperature, transition width, and residual resistance ratio. Surface roughness and film thickness were measured on selective films.

Sheet resistance (R_s), superconducting critical temperature (T_C), transition width (ΔT_C), and residual resistance ratio (RRR)

The room-temperature sheet resistance was measured using a home-built four-point probe connected to a Keithley 2400 source meter. The sample was probed at the center with different orientations, and the average result was taken.

The superconducting transition was measured using a home-built system with 8 4-point-probe channels in a Gifford-McMahon cooler. We swept the temperature by turning on and off the heater on the cold head. During the temperature sweeping, we sourced a 100 μA current, and continuously measured the voltage on the 8 channels.

Figure 3-2 shows a typical superconducting transition curve we measured (film number: SPE775). The superconducting transition is not a step function. It is smeared over a finite temperature interval because of statistical fluctuation in the ordering parameter that defines the states of metal [62]. In all of our characterization, T_C is defined to be the temperature where the resistance drops to 50% of resistance at 20 K (R_{20K}). ΔT_C is defined as temperature width between 90% and 10% R_{20K}. It is an indication of disorder. RRR is defined as R_{300K}/R_{20K}. It is related to the impurity in the material.

Figure 3-3 shows the range of parameters we obtained from different deposition runs. Based on previous experiences in fabricating saturated detectors on SiN_x [35], we aimed for a sheet resistance of 500-530Ω/sq, and optimized our process for higher T_C. The blue band covers the range of films that were used to produce saturated detectors. Though films with smaller sheet resistance had higher T_C, they were too thick to result in saturated detectors based on the 60-nm 2-SNAP design for 1550 nm

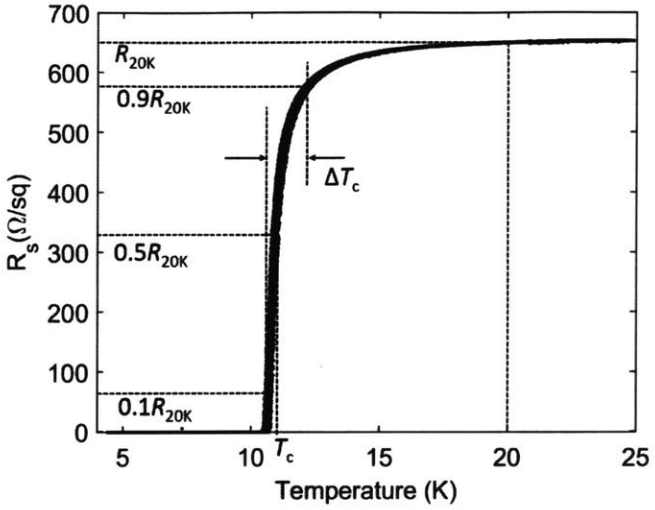

Figure 3-2: A typical superconducting transition curve (film number: SPE775). T_C is defined to be the temperature where the resistance drops to 50% R_{20K}. ΔT_C is defined as temperature width between 90% and 10% R_{20K}. RRR is defined as R_{300K}/R_{20K}.

illumination. These films have $T_C \approx 11$ K, $\Delta T_C \approx 1.8$ K, and RRR$\approx$0.84. These values are close to those of the films deposited on SiN_x substrates using the same deposition process.

Surface roughness

We measured the surface roughness of the AlN substrate using AFM. Figure 3-4 shows the AFM image scanned on a 1 μm×1 μm area. The root mean square (RMS) roughness was 0.726 nm. We observed evenly distributed "granular" structures with size ~30 nm. Figure 3-4(b) shows the size distribution of the grains. The peak at 2 nm was from the gap left over when we divided the grains, and did not reflect real grain size. The dimension of the grains (20-40 nm) was consistent with the nanocolumns reported in the literature for AlN on c-sapphire [63]. The reason we could not see the pyramidal shape for the nanocolumns was likely due to the AFM tip size (radius of curvature of ~10 nm), which convolved the actual shape of the nanocolumns.

After NbN deposition, the columnar features were transfered to the NbN film, and the RMS surface roughness decreased slightly to 0.56 nm (Film number: SPE769).

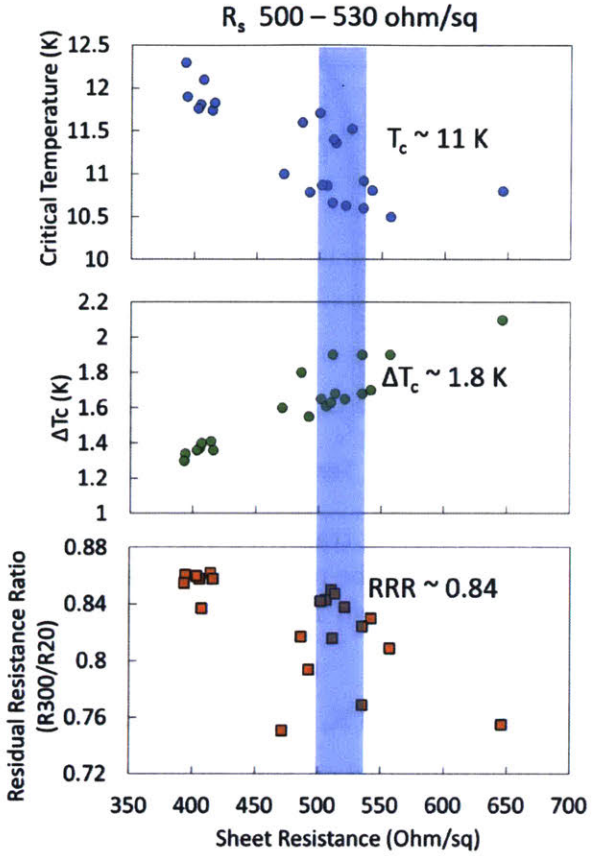

Figure 3-3: T_C, ΔT_C, RRR, and sheet resistances for NbN films from different deposition runs. The blue band covers the range of films that were used to produce saturated detectors. Though films with smaller sheet resistance had higher T_C, they were too thick to result in saturated detectors based on the 60-nm 2-SNAP design at 1550 nm radiation.

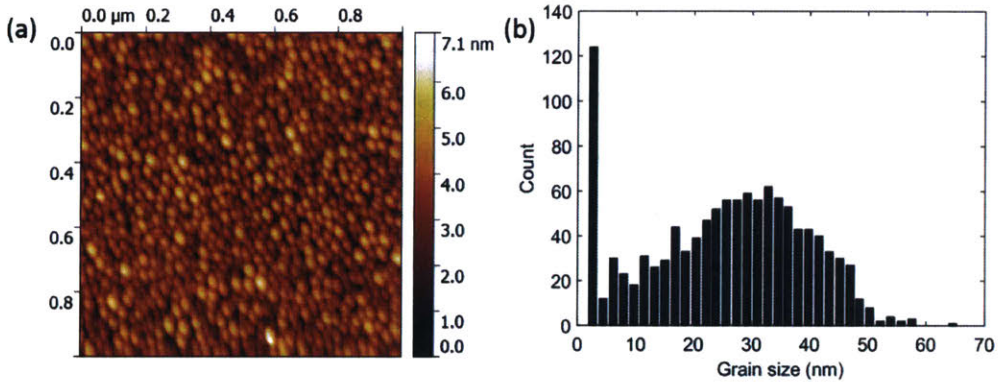

Figure 3-4: Surface topology of bare substrate. (a) AFM image of the bare substrate shows evenly distributed nanocolumns. (b) Size distribution of the nanocolumns.

Film thickness

To accurately measure the NbN film thickness, we etched a step on the film and measured the step size using AFM.

To create the step, we partially masked the film with photoresist (S1813), and etched away the NbN film using CF_4 reactive ion etching (50 W, 3 min, detailed process see Section 3.2.2). Since CF_4 reactive ion etching barely etches AlN (no measurable etch rate after a 5 min test etching), AlN serves as a natural etch stop. After stripping the photoresist, the NbN step was created.

Figure 3-5(a) shows the AFM image of the NbN step. On the left is AlN, and on the right is NbN. Figure 3-5(b) shows the histogram of the pixel height in Fig. 3-5(a). The film thickness, extracted as the separation of two the peaks, is 4.7 nm.

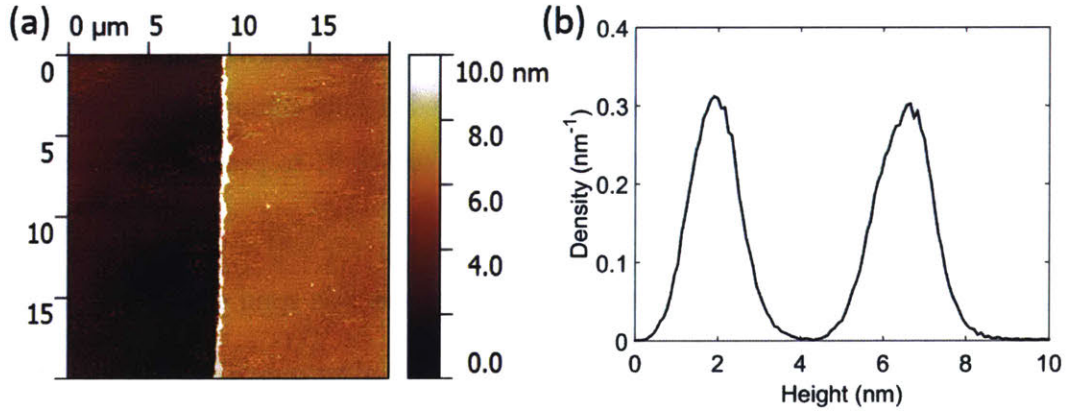

Figure 3-5: AFM measurement of film thickness. (a) AFM image of the step etched on the NbN film. (b) Histogram of the pixel height. The measured film thickness was 4.7 nm. (Device number: SPE769)

3.2 Detector Fabrication

The detector fabrication involves two parts. The first part is to pattern the gold electrical contact pads and alignment marks using photolithography followed by metal liftoff. The second part is to define the superconducting nanowires using electron-beam lithography, followed by pattern transfer through reactive ion etching.

3.2.1 Electrical contact pad and alignment mark patterning

A bi-layer lift-off process was used to define the gold contact pads and alignment marks (for simplicity, they will be referred as "gold pads" hereafter). The bi-layer process introduces an undercut layer, which greatly facilitates metal liftoff. Fig. 3-1(b) shows main process steps, and below gives a more detailed description.

1. Prior to applying photoresist, the substrate was cleaned using acetone and IPA during spinning.

2. Micromchem PMGI SF9 resist was spun coated to the sample at a speed of 3 krpm for 1 min. The sample was then soft-baked on a hotplate at 110 °C for 1 min.

   The PMGI is the undercut layer in the bi-layer process. It dissolves rapidly in TMAH based developers. By tuning the baking condition, one can control the undercut depth. Though the recommended baking temperature is around 180 °C, we restricted our baking temperature to 110 °C to prevent oxidation of the NbN film.

3. Shipley Microposit S1813 positive-tone photoresist was spun coated at 5 krpm for 1 min, and then baked at 80 °C for 1 min.

4. The sample was exposed in a UV contact photolithography system (Tamarack), with a dose of 30000 $\mu J/cm^2$. If the measured UV intensity is 1880 $\mu W/cm^2$, for instance, a 16 s exposure is needed. The photomask was fabricated using a mask writer (Heidelberg) in the NSL.

5. The exposed sample was developed in Microposit MF CD-26 developer (2.4% TMAH) for 20 s, rinsed in flowing DI water for 45 s, and blown dry using N_2 gas.

   Since the PMGI was baked at a relatively low temperature, its undercut rate was higher than the specified values. An over-development will cause over-undercut, which may completely lift off some small structures. Fig. 3-6 shows

an optical micrograph of an over-undercut sample. The background color was red because the light source of the microscope was filtered so that the resist would not be exposed during imaging. The darker region was the exposed area, where resist was developed away; and the lighter region was the non-exposed region, where resist still remained. A clear undercut layer was observed between the two regions. Because the sample was overdeveloped and the undercut was too much, the letter "E" was lifted off.

Figure 3-6: Optical micrograph of an over-undercut sample, where small structures peeled off.

6. A stack of 5 nm Ti/50 nm Au/5 nm Ti/50 nm SiO_2 was deposited on the sample using electron-beam evaporation. Ti was used as an adhesion layer for Au. Normally, a 10 nm Ti/25 nm Au stack is enough for electrical contact. Our waveguide fabrication process, however, involves chlorine-based ICP etching, which would destroy the 10 nm Ti/25 nm gold pad. We therefore added a 50 nm SiO_2 layer to protect the gold pads. We also made the gold layer thicker to enhance imaging contrast in EBL alignment.

7. In the final lift-off step, the sample was first sonicated in acetone for 3 min, followed by methanol and IPA rinse, and blown dry with N_2. Then, the sample was dipped in CD-26 for 2 min, followed by a DI dip for 1 min. In fact, the PMGI layer can be completely dissolved in less than 30 s in the CD-26, but we found that increasing the CD-26 dipping time can help promote adhesion

between the electron-beam resist and the substrate.

3.2.2 Nanowire patterning

The superconducting nanowires were defined using EBL with a negative-tone electron-beam (e-beam) resist, hydrogen silsesquioxane (HSQ). The HSQ pattern was transferred to the NbN film using reactive ion etching (RIE) with fluorine chemistry. The major steps are depicted in Fig. 3-1(c).

HSQ spin curve

For SNSPD patterning, we used 4% HSQ. The HSQ is stored in a fridge using 1.5 mL high-density polyethylene vials. Before spin coating, we warm the HSQ vial using hand for about 10 min until it reaches room temperature, and let it rest in ambient temperature for 1 min. For large bottles (e.g., 125 mL), it takes ~1.5 hours for warming. This step prevents water vapor from condensing in the HSQ. We occasionally observed serious contamination (junk spreading over patterned structures after exposure and development) when the ambient humidity was high during resist spin.

Figure 3-7 shows the spin curve measured on bare silicon substrate (1 cm × 1 cm chip). The plot was based on 30 data sets over a period of 8 months. The spin time was 60 s; for each chip, 4 drops of resist was applied. The thickness was measured using a broadband reflectometer (Filmetrics F20). The error bar indicates standard deviation. Slow acceleration and fast acceleration corresponds to nominal rates of 1 krpm/s and 9 krpm/s, but the actual acceleration is not calibrated.

We noticed that faster acceleration gave thinner film. This acceleration-dependence usually does not happen for thick films or large substrates. It may suggest that the resist has not settled to its stable thickness; or the initial resist spreading does affect the final film thickness for such small substrate and thin resist. We also observed large variation of resist thickness (~10 nm). This variation may due to the accuracy of the measurement tool, or refractive index change of HSQ. We note tendency of increased refractive index of aged HSQ, but the data we have are not yet conclusive. Despite

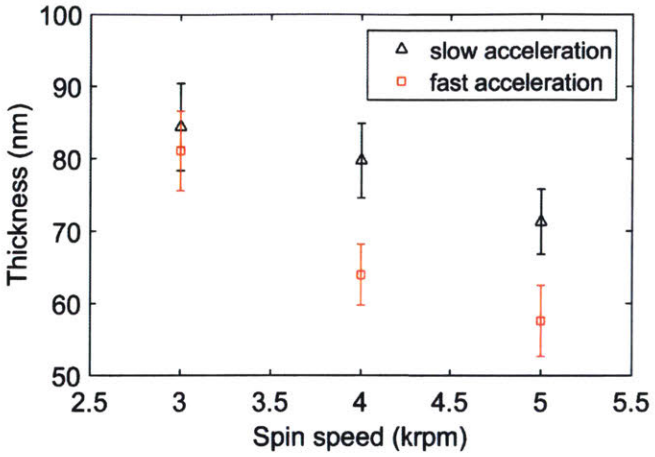

Figure 3-7: Spin curve for 4% HSQ on 1 cm×1 cm silicon chip. Slow and fast acceleration corresponds to nominal rates of 1 and 9 krpm/s, but the actual rate is not calibrated.

the variation of film thickness, the e-beam dose, especially for a 125 keV system, is barely affected. In our fabrication process, we used 4 krpm spin speed and 9 krpm/s nominal acceleration.

We always spin HSQ right after gold pad liftoff, when the surface is still clean and activated. After spin coating, we go for e-beam exposure immediately, because HSQ will otherwise cross link spontaneously. When HSQ is "old," it become more sensitive and requires less dose.

E-beam exposure

The e-beam resist was exposed using a 125 kV EBL system (Elionix ELS-F125). The exposure parameters are listed Table 3.1. We used 200 pA beam current to expose the nanowires, and 2 nA to expose the inductors and large leads. This method greatly reduced the total exposure time. The exposure was aligned to the registration mark defined on the gold pads using the "reg-2" manual alignment.

Table 3.1: Parameters for e-beam exposure of SNSPDs

Write field: 500 μm	Beam current: 200 pA (nanowire) & 2 nA (inductor, lead)
Dot map: 200,000 dots	Dose time: 1.2 μs/dot (200 pA) & 0.12 μs/dot (2 nA)
Dot size: 2.5 nm/dot	Area dose: 3840 $\mu C/cm^2$

Proximity correction was not performed because the nanowires were sparse. During exposure, the chip was clipped to the metal stage and established good electrical contact. The NbN film and the gold pad structures helped in reducing charging effect. Without the NbN film and gold pads (e.g., when pattering AlN waveguide structures without detectors), we did observe serious charging effect. In this case, e-spacer was needed.

The e-beam dose changes over time due to the aging of HSQ. We periodically write dose matrix to check the dose. The standard dose matrix consists of NbN nanowires with different width (30 nm, 60 nm, and 100 nm) and filling ratio (1:1 and 1:3), and with both horizontal and vertical orientations. Our critical structure (i.e., 60 nm parallel nanowires) was also included to the dose matrix. Figure 3-8 shows a unit cell of the dose matrix.

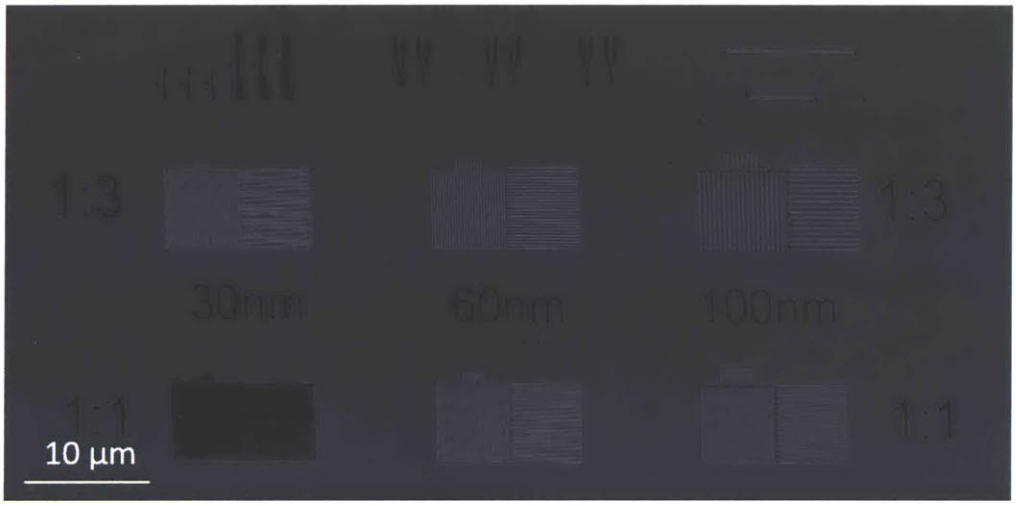

Figure 3-8: SEM of a unit cell of the standard dose matrix. The original pattern was designed by Adam McCaughan.

On each detector chip, besides the intended detectors, we patterned test structures for diagnostic purposes. These structures include 3 μm×3 μm standard SNSPD (as a standard reference), nanoSQUID (can be used to measure kinetic inductance) [64], and 1 μm strip (can be used to measure critical current density). Figure 3-9 shows an SEM of a set of test structures.

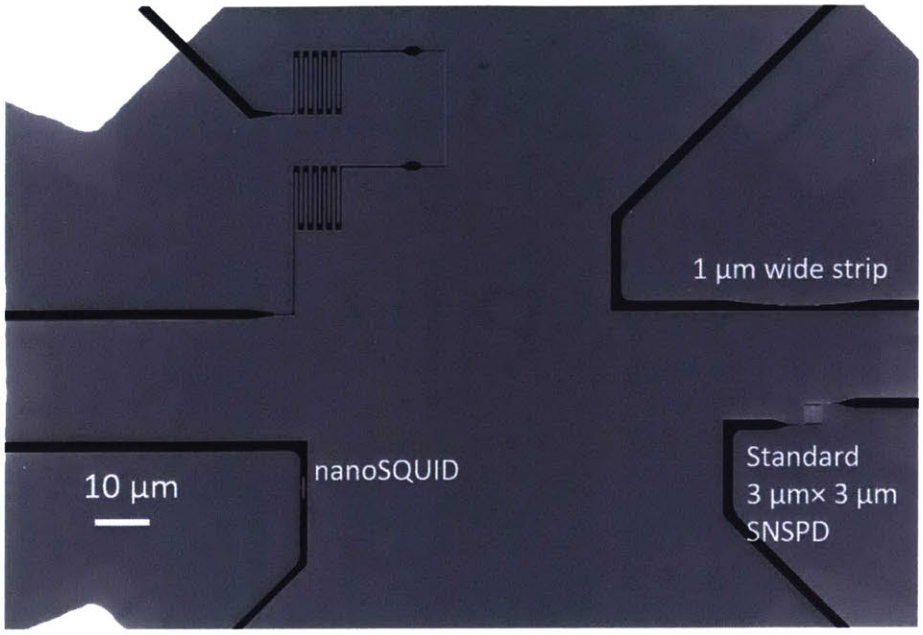

Figure 3-9: SEM of a set of standard test structures for diagnostic purposes.

Resist development

The exposed sample was developed in 25% TMAH for 2 min, and then rinsed in DI water for 45 s. Before blown dry in N_2, the sample was dipped in IPA for 10 s. Since IPA has a smaller surface tension compared to DI water, structures with high aspect ratio are less likely to collapse during the drying process.

It is worth noting that most of the chemical reaction happens in the first 30 s during the development. And we observed that a 45 s development time was already enough to remove the unexposed HSQ. The additional development was to make sure no residual was left, and ensure a good contrast.

Figure 3-10 shows an SEM of the patterned HSQ structure after development. The dark part is HSQ, the gray part is NbN, and the bright part is gold pad. The insets show the zoomed view of the nanowire and inductor.

Reactive ion etching (RIE)

The HSQ pattern was transfered to the NbN film using RIE. During etching, the chamber was at a pressure of 10 mTorr, and the He and CF_4 gases were flowing into

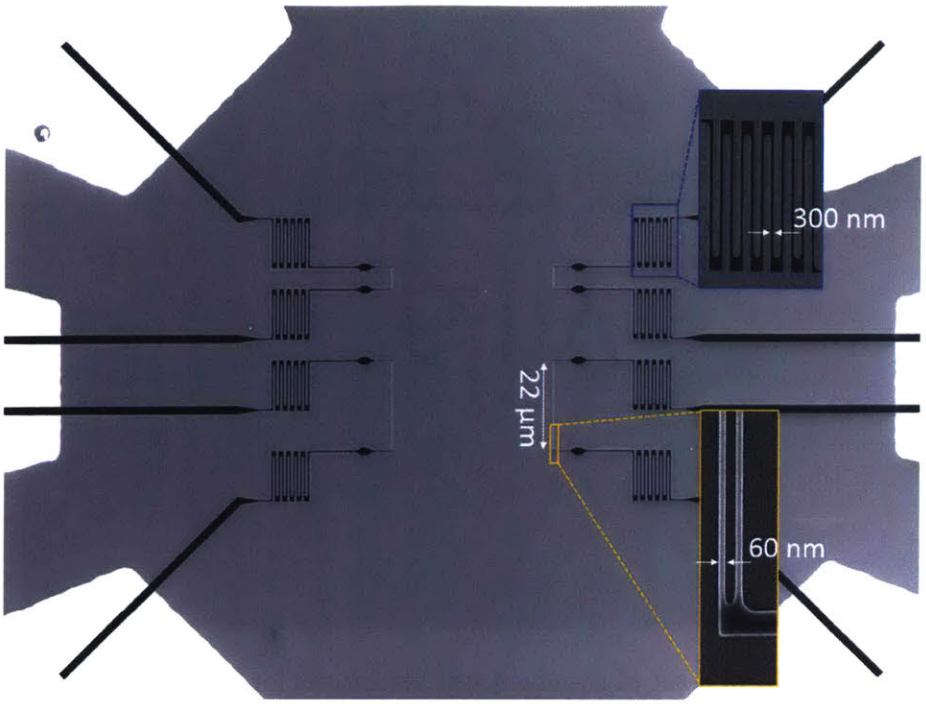

Figure 3-10: SEM of the patterned HSQ etch mask of the SNSPD. The inset shows the zoomed view of the inductor (upper) and parallel nanowires (lower).

the chamber at a rate of 7 sccm and 15 sccm, respectively. The power was set to be 50 W. A cleaning etch with O_2 and CF_4 is recommended if the chamber is dirty.

Controlling the etch process is critical, because an over etch will result in side-wall etching and rough edges on the NbN nanowire, and affects the device yield. However, even when the process parameters are set the same, the etch rate drifts over time, especially after major equipment maintenance. A regular monitoring of the etch rate is necessary, and the etch time can be tuned according to the measured etch rate.

Directly measuring the etch rate on the few-nm-thick NbN films is difficult. Instead, we placed a dummy SiO_2-on-Si sample next to the NbN sample during etching, and measured the thickness of the SiO_2 before and after etching using a reflectometer (Filmetrics F20). Since the refractive index of SiO_2 and Si are accurately known, the thickness of the SiO_2 can be measured with a high accuracy (< 1 nm). We started with a 255 nm SiO_2 on Si substrate, and used it to monitor the etch rate continuously until it was thinner than 30 nm, then replaced it with a new 255 nm SiO_2-on-Si dummy sample.

The initial searching for the optimal etch time was done by an incremental "etch and inspect" method. That is, after the first 1 min (the NbN was not completely etched yet), we inspected the NbN structures after every 15 s etch. The inspection was by resistance measurement (measuring the resistance of the nanowire and designed open junctions) and SEM imaging (by observing charging effect around the nanowires).

Figure 3-11 shows the measured etch rate on the SiO_2-on-Si dummy samples. The plot contains a set of 28 data points over a period of 9 months. The etch rate has a mean of 10.2 nm/min, and standard deviation of 0.77 nm/min. The difference between the highest and lowest etch rates is 3 nm/min. Most of the data points were measured at an etch time of 2 min. It is worth mentioning that the etch rate is nonlinear—We observed a higher etch rate at the beginning of the etch.

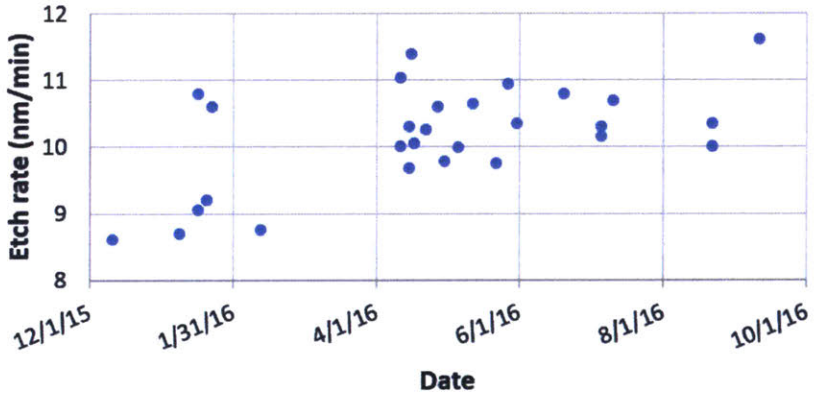

Figure 3-11: Etch rate of CF_4 RIE measured on SiO_2-on-Si dummy samples.

3.3 Photonic Circuit Fabrication

The main fabrication process for low-loss AlN waveguide for visible wavelength was developed by Tsung-Ju Jeff Lu. 2% HSQ was spun coated at 2 krpm for 60 s with a nominal acceleration of 1 krpm/s. The e-beam exposure was aligned to the same alignment marks used for the SNSPD patterning. We used 1 nA beam current to write the grating couplers and waveguide, and used 5 nA beam current to write the leads that

cover the superconducting inductor and leads. The area dose was 9000 $\mu C/cm^2$. The exposed HSQ was developed in salty developer(1 wt% NaOH + 4 wt% NaCl [65]) for 2 min 40 s, and rinsed with DI water and IPA. The chip was etched using inductively-coupled plasm (ICP) etching with chlorine chemistry.

Figure 3-12 shows an SEM of the HSQ mask for the waveguide aligned to the detectors. The middle waveguide was for calibration purpose.

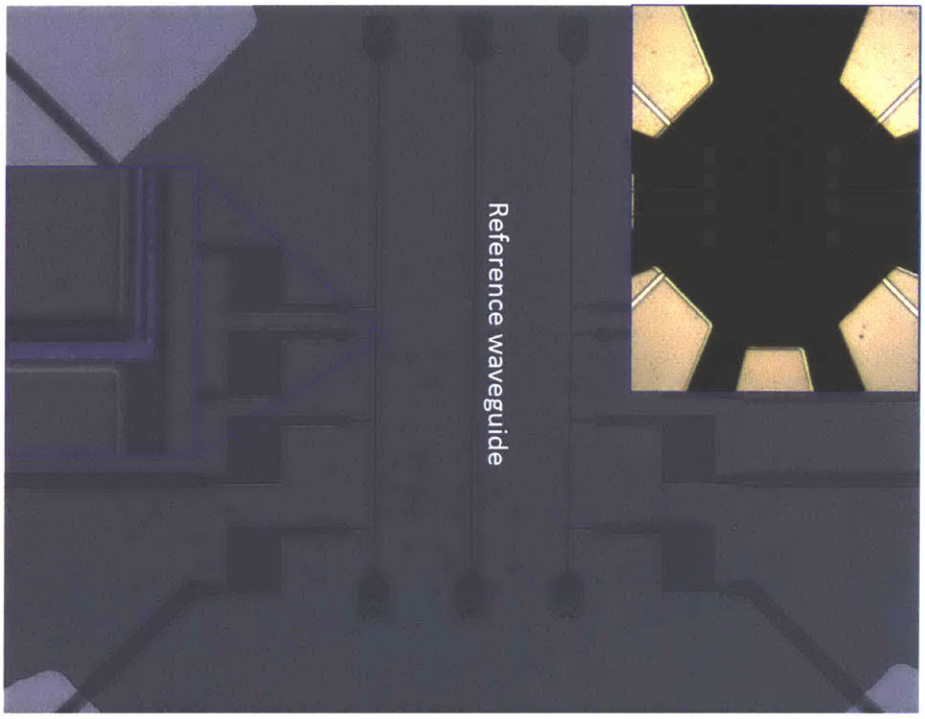

Figure 3-12: AlN waveguide with integrated SNSPDs. The inset on the left shows the zoomed view of the alignment between waveguide and detector. The inset on the upper-right conner shows an optical micrograph of the same area after etching.

Figure 3-13 shows other AlN PIC components, including gratings, ring resonators (to measure waveguide loss), filters (to filter pump light), and taper (for diamond membrane integration).

3.4 Challenges and Common Problems

HSQ adhesion problem. Bad adhesion between HSQ and NbN has long been a problem, especially for narrow, long nanowires. Figure 3-14 shows some examples of

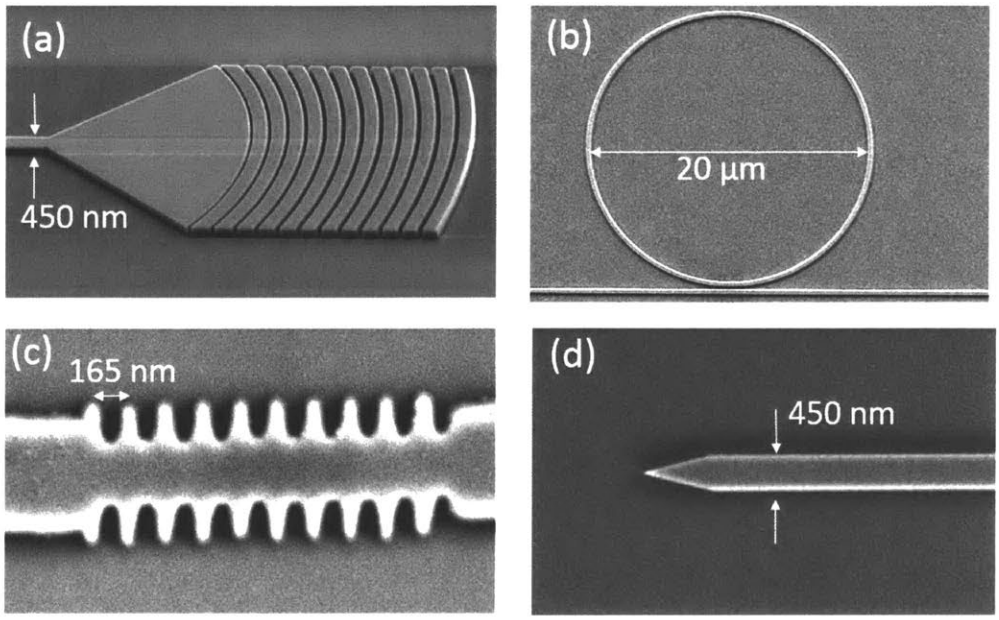

Figure 3-13: AlN PIC components. (a) Grating coupler; (b) ring resonator; (c) waveguide filter; and (d) waveguide taper. Images are from Tsung-Ju Jeff Lu.

bad adhesion.

There are several methods that may improve HSQ adhesion:

1. HSQ adheres well with SiO_2, so a thin SiO_2 buffer layer can help with adhesion.

2. O_2 plasma ashing can help activate the surface and provide better adhesion. However, it will oxidize NbN film.

3. TMAH, which is the developer for HSQ, can promote adhesion. In our fabrication process, we dip the chip in CD-26 (2.4% TMAH) for 2 min for adhesion promotion.

4. We found that adhesion was generally good for fresh HSQ, but became bad when HSQ aged. Keeping track of the HSQ condition and restocking promptly would be helpful.

Process compatibility. Process compatibility is critical in multi-material, multi-step processes. Gold pad protection was an issue in our process. Chlorine ICP etching

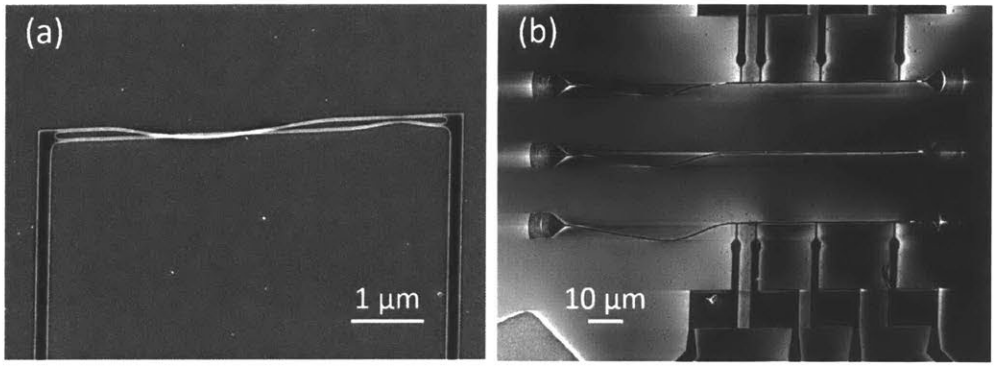

Figure 3-14: Examples of bad HSQ adhesion.

will destroy unprotected gold pads, and contaminate the etcher. We considered Al_2O_3 and SiO_2 for gold pad protection. Evaporated thin alumina protection can survive both fluorine (for SNSPD) and chlorine (for waveguide) etch, but it will crack in HSQ salty developer (strong base). Thin SiO_2 can survive in base and chlorine ICP etching, but it will be etched by fluorine RIE. In our final process, we used SiO_2 with just enough thickness that survives both etch steps, and the residual thickness is thin enough to allow wire bonds to penetrate. To prevent oxidation of NbN nanowires, we also reduced O_2 plasma clean time for waveguide fabrication.

EBL alignment. We defined alignment marks and gold pads in a single photolithography and metal lift-off step. This way, we can fabricate gold pads for many chips in one batch. This is very effective for fast prototyping and quick process development, in which no one expects to succeed at the first try (described as "expected failure" by my advisor, Karl Berggren).

Photolithography is fast, but the problem is its poor resolution. The alignment marks defined using photolithography are large and rough. It makes EBL alignment difficult, because the alignment relies on edge detection. Also, different tools have different dimension references, e.g., the dimension defined in the photomask (using the Heidelberg mask writer) may differ from the dimension defined by the laser interferometer in the Elionix. Ideally, we should define the marks using EBL as well.

EBL height sensor error. In the Elionix, focusing and stigmation are performed on an internal reference instead of directly on the chip. Once the correct focusing distance is registered, the laser height sensor will measure and adjust the stage height dynamically during writing. The height sensor makes measurement for each writing field. If it fails, it will adopt the height information from the previous writing field. Though Elionix has high acceleration voltage (125 kV), which gives a relatively large depth of focus, if height sensor does not work properly, serious out-of-focus will occur and affect the exposed pattern.

Figure 3-15 (a) shows how the height sensor works. A laser beam (spot size of 150 μm) is reflected off a flat substrate and recorded in real-time by a CCD camera. The position of the recorded Gaussian peak is directly related to the substrate height. A common situation that may cause height sensor error is when the laser beam hits the edge of the gold pads, which diffracts the laser beam and confuses the tool (see Fig. 3-15(b)).

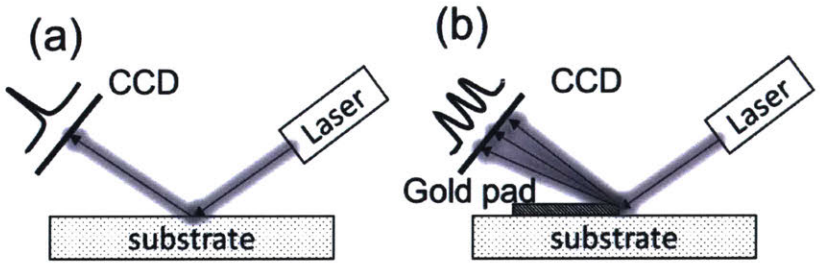

Figure 3-15: Height sensor error when the laser beam hits gold pad edge. (a) When a sample is flat, reflected beam is recorded by the CCD camera as a perfect Gaussian shape, and its position indicates the offset of the stage height. (b) When the laser beam hits the edge of the gold pads, the beam is diffracted and multiple peaks show up on the CCD camera, confusing the height sensor.

To solve the problem, we found two solutions. The first is to disable the real-time height sensing; and instead, measure the sample height and inclination manually. The second way is to shift the center of the writing field (this can be defined using the Beamer tool). We know that the laser spot is always at about 100 μm from the center of the writing field. By purposely shifting the defined writing field, we can avoid the laser spot from hitting on the gold pad edge. Or, alternatively, we can offset the laser

spot (can be defined in the Wecas tool).

I am not sure anyone would read the thesis to this point,[1] but I have an important advice based on my own experience: Do not drink coffee right before fabrication. Dropping a chip, that you have spent weeks on, on the floor, and facing down, is frustrating. And most likely, when you pick it up, it will drop again.

[1] It turns out that my advisor did.

Chapter 4

Measurement and Result

In this chapter, we describe the measurement apparatus and results, with focus on the basic detector metrics, including hysteric I-V curve, pulse shape, detection efficiency, and timing jitter. The results reported here are for SNSPDs on un-patterned AlN substrate. Though we have fabricated SNSPDs on AlN PICs, these devices have not been measured systematically, and we are not able to report accurate on-chip detection efficiencies.

4.1 Cryostats

Two cryostats were used in this project: the Lake Shore cryogenic probe station, and the Montana microscope-coupled cryostat. The probe station was used to screen the devices and characterize the basic detector metrics. The Montana was intended to be used for measuring the on-chip detection efficiency of the waveguide-integrated detectors.

Lake Shore cryogenic probe station. The Lake Shore cryogenic probe station is cooled by flowing liquid helium, which brings the cold head to 4.2 K (the temperature on the sample holder is 4.9 K); and by pumping the helium, the cold head can reach a stable base temperature of 1.5 K, and the sample holder can reach a stable temperature of 2.5 K.

Figure 4-1 shows a top-down view of the inner vacuum chamber of the probe station. The sample holder is mounted to the cold head with indium foils applied on the bottom. It holds the sample vertically so that fiber probe can illuminate the chip from the back. The RF probe comes from the side, and probes the chip in the front. A silicon diode temperature sensor is installed on the chip holder.

A high numerical aperture (NA) fiber is attached on a feed through mounted on an x-y translational stage. The fiber probe can move parallel to the sample surface, accessing all devices. The output power and beam profile are calibrated (see Appendix A) so that we can estimate the photon rate landing on the devices.

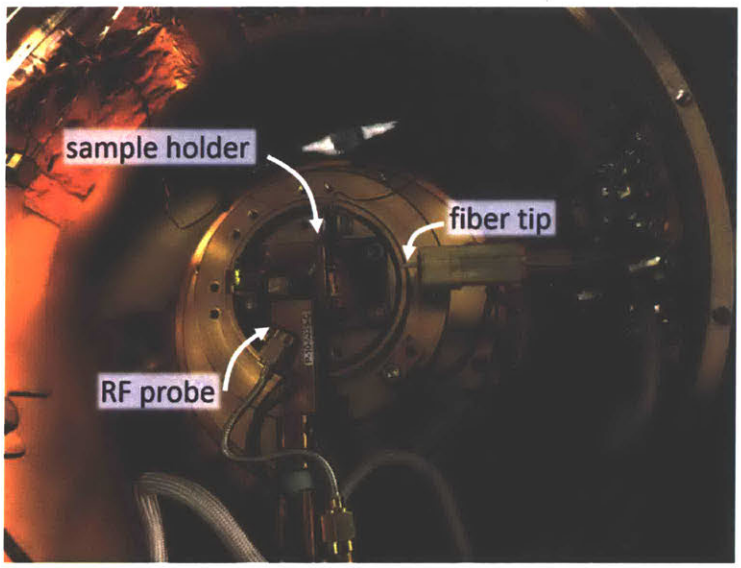

Figure 4-1: Inner chamber of the Lake Shore cryogenic probe station. The sample holder holds the chip vertically, and the fiber illuminates the chip from the back.

Montana microscope-coupled cryostat. The Montana cryostat is a Gifford-McMahon cryocooler with a base temperature of 3.7 K, and the temperature can be controlled through a feedback loop. The Montana cryostat is designed for confocal microscopy with low drift and vibration. It has an objective lens inside the vacuum chamber, and the chip sits on a three-axis piezostage (Attocube). The Montana cryostat is compact and has very limited chamber space. Hyeongrack Choi and I made a sample holder to host the chip and the printed circuit board (PCB). The

sample holder was made from oxygen-free copper, and coated with gold to prevent oxidation and enhance thermal contact. The PCB can host 6 RF channels. To save space, we used UMC connectors. The chip is attached to the sample holder using silver paste, and devices are wire bonded to the PCB.

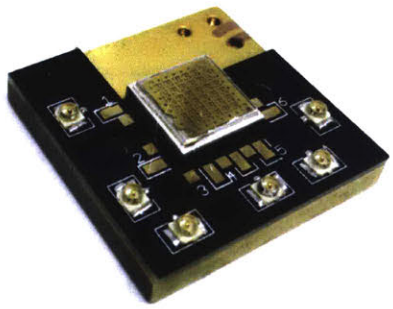

Figure 4-2: Sample holder made for the Montana cryostat. The detector directly sits on top of the gold-plated copper mount for better thermal link. The PCB was designed to host 6 RF-channels with UMC connector. The chip at the center is 1 cm×1 cm.

4.2 DC Hysteretic I-V Curve Measurement

Figure 4-3 shows a simplified circuit diagram for the IV curve measurement. The full biasing circuit is shown in Fig. 4-9, and we replaced the RF readout using a 50 Ω terminator. At DC, we treat the inductor to be short and capacitor to be open. The bias voltage, $V_{\rm b}$, was supplied using an isolated battery source (Stanford Research Systems). The battery source was connected to a 100 kΩ resistor, $R_{\rm b}$, to provide current bias to the detector (denoted as the symbol "S"). A multimeter (Keithley 2700) was used to measure the voltage across the detector. Since the multimeter has a large input resistance (10 GΩ), we can neglect the current flowing into the multimeter branch, and the measured voltage, $V_{\rm s}$, is approximately the voltage across the detector, $V_{\rm d}$. The 1 MΩ resistance was inserted to block the noise from the multimeter.

The voltage and current on the detector follows the relation:

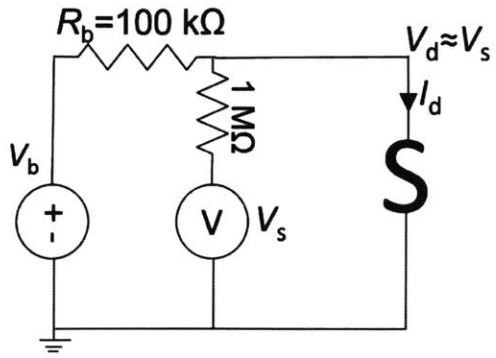

Figure 4-3: Simplified circuit diagram for the DC biasing circuit.

$$I_{\mathrm{d}} = \frac{V_{\mathrm{b}} - V_{\mathrm{s}}}{R_{\mathrm{b}}} \tag{4.1}$$

Figure 4-4 shows a measured hysteretic I-V curve of a 5-μm-long 2-SNAP. The measurement was done in the Montana cryostat at 3.8 K. (Device number: SPE768-4B3; measurement was performed four months after the initial characterization in the probe station, so some degree of oxidation might have happened.) The I-V curve was obtained by ramping up the bias voltage from 0 until the nanowire fully switches to normal state, then ramping down to the opposite polarity, and finally return to zero. When the biasing current is smaller than the switching current (I_{sw}), the detector is superconducting, and there is no measurable voltage on the detector. When the biasing current increases beyond I_{SW}, the detector switches to normal state. The solution of Eq. 4.1 gives the load line (see Fig. 4-4), which determines which resistive state the nanowire switches to. When reducing the voltage on the nanowire, there is a region where current holds constant. This region is called hotspot plateau, and the corresponding current is called hotspot current or retrapping current [53]. The retrapping current can be used to estimate the thermal boundary conductance.

The multiple switching points are due to the switching of different sections on the detector (the 60-nm-wide parallel nanowires and 200-nm-wide lead). This explanation is confirmed by the ratio between the two retrapping current ($I_{\mathrm{n1}}/I_{\mathrm{n2}} \approx 0.6$), which agrees with the ratio of the nanowire width, $2 \times 60\,\mathrm{nm}/200\,\mathrm{nm}$. And this ratio roughly holds for various temperatures (see Fig. 4-6). The reason why the multiple switching

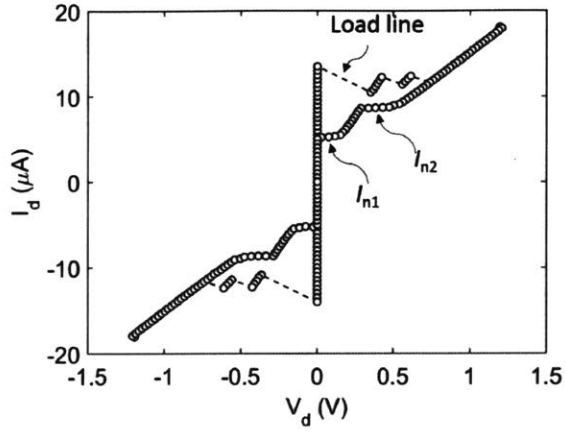

Figure 4-4: IV-curve of waveguide-integrated 2-SNAP. Multiple switching points and retrapping currents were due to the switching of different regions of the detector. (Device number: SPE768-4B3)

points do not follow this ratio is likely because the hot nanowire (which switched first) suppressed the I_{SW} of the leads.

Figure 4-5 shows a series of I-V curves of the same nanowire at different temperatures. The labeled temperatures were readings on the sample stage. The actual temperature on the chip was higher than that due to thermal load of the sample holder and RF cables.

We extracted the two retrapping currents, I_{n1} and I_{n2}, at different temperatures, and plot them in Fig. 4-6. We noticed that the temperature-dependent retrapping current did not fit the formula derived in [53] ($I_{\mathrm{h}} = (\alpha W^2 T_{\mathrm{C}} d/\rho)^{1/2}(1-t)^{1/2}$, where $t = T_{\mathrm{sub}}/T_{\mathrm{C}}$). The same observation was reported in [47]. Nevertheless, the ratio between I_{n1} and I_{n2} holds ~ 0.6 and did not vary with temperature.

We tried to fit the measured temperature-dependent switching current using the Ginzburg-Landau theory, $I_{\mathrm{sw}}(T) = I_{\mathrm{sw}}(0)(1-t^2)^{3/2}(1+t^2)^{1/2}$, where $t = (T_{\mathrm{stage}} + \Delta T)/T_{\mathrm{C}}$. Here, T_{stage} refers to the temperature reading on the samples stage, and ΔT refers to the temperature difference between the sample stage and the chip. Figure 4-7 shows the fitting. $I_{\mathrm{sw}}(0) = 17.39\,\mu\mathrm{A}$, $\Delta T = 1.39\,\mathrm{K}$, and $T_{\mathrm{C}} = 11\,\mathrm{K}$ give the best fitting. However, ΔT of 1.39 K seems to be too large; and we do understand that the switching current of a nanowire is limited by many factors and is usually much smaller than the de-paring current.

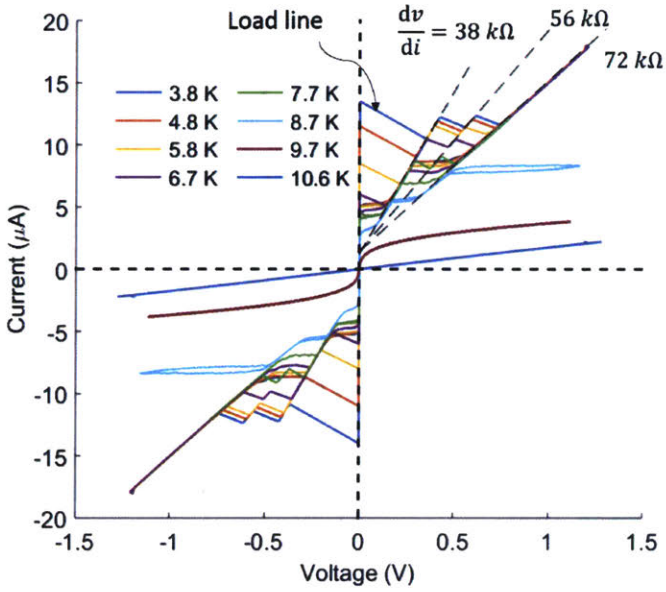

Figure 4-5: IV-curve measured at different temperatures. The temperatures labeled were readings on the sample stage; the actual sample temperature was higher. (Device number: SPE768-4B3)

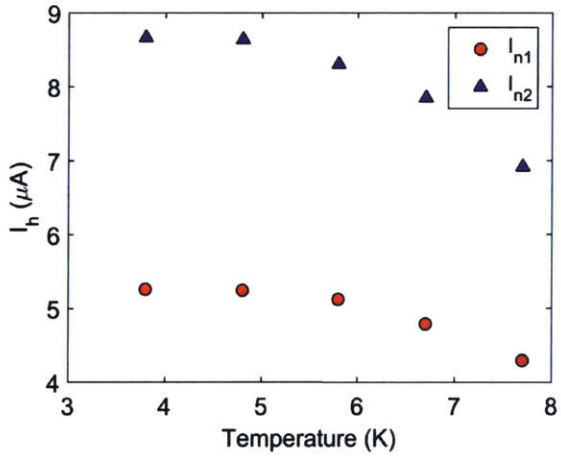

Figure 4-6: Retrapping currents measured at different temperatures. I_{n1} and I_{n2} are the two hotspot currents as labeled in Fig. 4-4. Data are extracted from Fig. 4-5.

4.3 Detection Efficiency (DE) Measurement

Figure 4-8 depicts the setup for DE measurement. The optical input was split into two arms, one sent to an optical power meter, and one sent to the SNSPD. The light going to the detector was attenuated using a variable optical attenuator to single

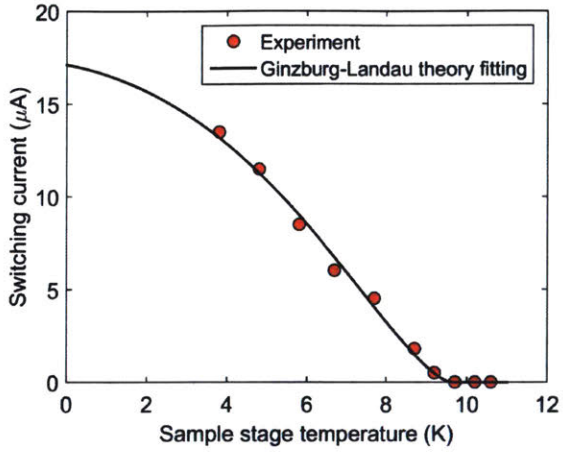

Figure 4-7: Switching current vs. temperature. The dots are experimental results, and the line is fitted using Ginzburg-Landau theory ($I_{\rm sw}(T) = I_{\rm sw}(0)(1-t^2)^{3/2}(1+t^2)^{1/2}$, where $t = (T_{\rm stage} + \Delta T)/T_{\rm C}$). ΔT was to compensate the difference between the measured stage temperature and actual temperature of the sample. $I_{\rm sw}(0) = 17.39\,\mu$A, $\Delta T = 1.39\,$K, and $T_{\rm C}= 11\,$K give the best fit.

photon level, i.e., $P(2) \ll P(1)$.[1] The polarization was tuned to maximize detector counts. A 6 GHz oscilloscope (Lecroy WP760Zi) was used to record the output pulse. When measuring counting rate, a 225 MHz universal counter (Agilent 53131A) was used.

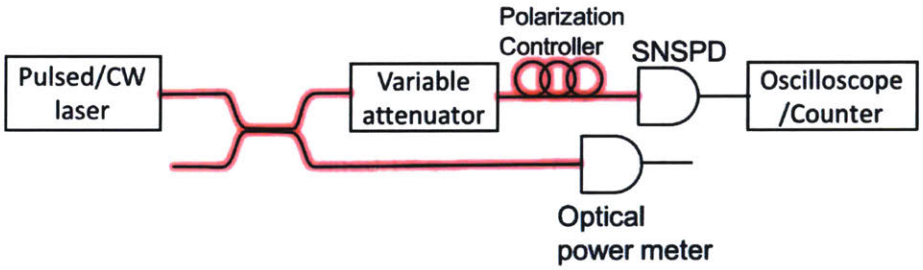

Figure 4-8: Schematics for the DE measurement setup.

Figure 4-9 shows the biasing circuit for the SNSPD. The voltage was supplied using an isolated battery source (Stanford Research System), the bias tee was from Mini-Circuit (ZFBT-6GW+). When measuring pulse shape and DE, we used a 1 GHz

[1] For coherent state, $|\alpha\rangle = \sum_{n=0}^{\infty} \frac{\alpha^n}{\sqrt{n!}} e^{-|\alpha|^2/2}|n\rangle$, where $|n\rangle$ is the number state (or Fock state), and $|\alpha|^2$ is the mean photon number. The probability of having k photon is $P(k) = |\langle k|\alpha\rangle|^2 = \frac{|\alpha|^{2k}}{k!} e^{-|\alpha|^2}$. When $|\alpha| \ll 1$, $P(2)/P(1) = |\alpha|^2/2 \ll 1$

amplifier (MITeq AM-1634-1000); and when measuring jitter, we used two cascaded 2.5 GHz amplifier (RF BAY LNA2500). To reduce reflection from the amplifier, we inserted a 3 dB attenuator before the amplifier.

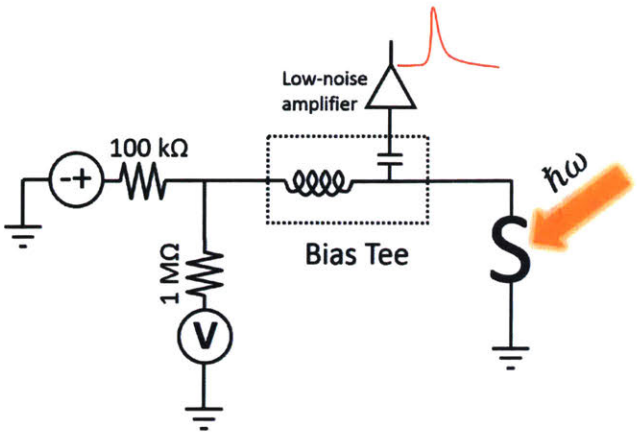

Figure 4-9: Biasing circuit for SNSPD.

Figure 4-10 shows a single-shot oscilloscope trace of the voltage pulse from the detector. The measurement was done in the probe station at 2.45 K. We fit falling edge of the pulse using an exponential function, and found the decay time constant to be τ=1.95 ns, which corresponds to a reset time of $3\tau \approx$5.85 ns.

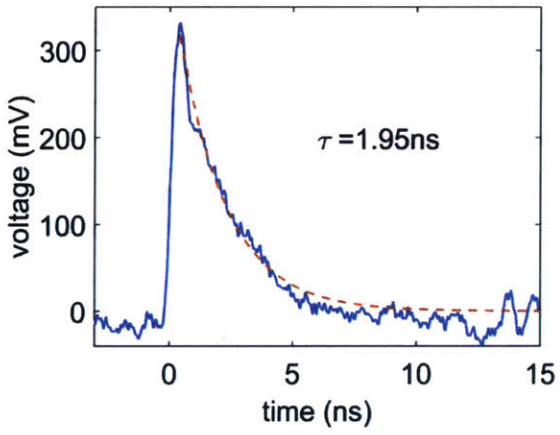

Figure 4-10: A single-shot oscilloscope trace of the output pulse from the detector. (Device number: SPE768-4B3)

When measuring counting rate, we biased the device to 90% I_C, and scanned the trigger level of the counter. We set the trigger level to the middle point of the flat

region in the count rate vs. trigger level curve. This level is approximately at 50% between the noise floor and pulse height.

Figure 4-11 shows the measured device detection efficiency (DDE) and background count rate (BCR). The measurement was done at 2.45 K with 1550 nm illumination. The photon flux shining on the back of the chip inside the active area of the detector was 62.1 Mph/s. The DDE was calculated as DDE = PCR/R_{ph}, where PCR is the photon count rate, R_{ph} is the photon rate on the device. The BCR was measured when the beam was blocked; PCR was measured when the beam blank was open, then subtract the BCR. The BCR included both intrinsic dark count (DCR) of the detector as well as the detection of background radiation. The high BCR was likely to be dominated by the background radiation, since similar level of BCR was measured in the system on low intrinsic DCR SNSPDs, which was tested in another well-shielded closed-cycle cryostat. Here, the photon rate was estimated by assuming the active area of the device to be 5 μm×200 nm (60-nm-wide parallel nanowire with 80 nm gap). The low DDE was due to the unpolished back surface of the chip, which scattered more than 60% of the incident light. The absolute value of DE here was not of our interest, because the detectors were designed for waveguide integration, which will have significantly higher absorption.

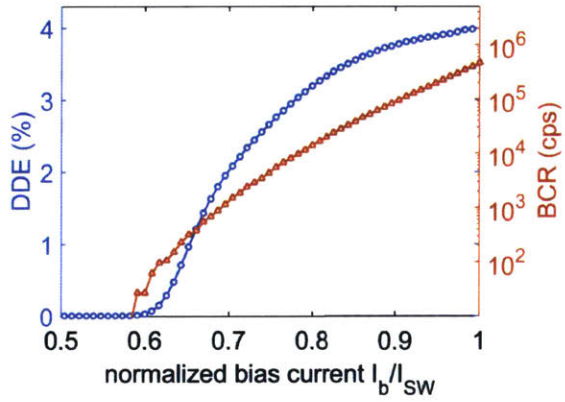

Figure 4-11: Back-illuminated DDE and BCR vs. I_{b} measured at 2.45 K with 1550 nm illumination. The DDE enters a saturation when I_{b} approaches I_{SW} with S = 0.16 (Device number: SPE768-4B3, I_{SW}= 23.5 μA.)

As we can see in Fig. 4-11, the DDE enters a saturation region as bias current

approaches switching current, with a saturation parameter $S = 0.16$. The saturation parameter is defined as $S = [I_{\mathrm{SW}} - I_{\mathrm{b}}(0.9\mathrm{PCR}(I_{\mathrm{SW}}))]/I_{\mathrm{SW}}$, where $I_b(0.9\mathrm{PCR}(I_{\mathrm{SW}}))$ is the bias current at which the PCR reaches 90% of its maximum value [35].

Figure 4-12 shows the normalized DE vs. I_{b} curves at different photon attenuations. The DE curves overlap after the avalanche current, indicating that the detector was working at single-photon regime. The photon-rate-dependent DE before the avalanche current is consistent with that observed in [49, 66, 35]).

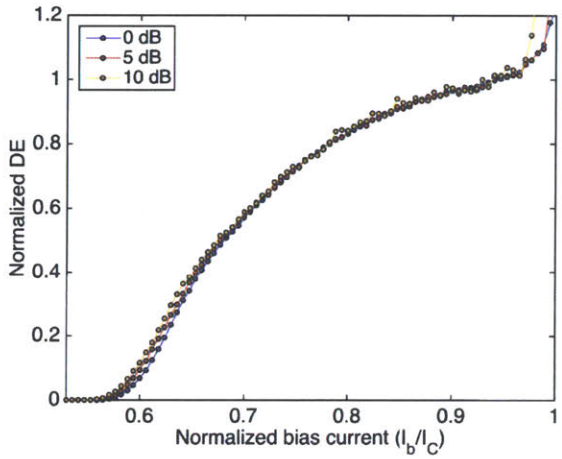

Figure 4-12: Detection efficiencies measured under different photon attenuations, confirming that the detector operated in single-photon regime.

We also measured the detector with different photon energies. As we can see in Fig. 4-13, as photon energy increases, the saturation behavior becomes more prominent, with increasing S parameter of 0.17 ($\lambda = 1550\,\mathrm{nm}$), 0.30 ($\lambda = 1064\,\mathrm{nm}$) and 0.33 ($\lambda = 780\,\mathrm{nm}$).

4.4 Jitter Measurement

Figure 4-14 depicts the setup for jitter measurement. The jitter was measured using a femtosecond pulsed laser at C-band (Calmar), which has a repetition rate of 20 MHz. The laser output was split into two arms, one to the SNSPD, and one to a 5 GHz fiber-coupled InGaAs photodetector (Thorlabs DET08CFC).

The oscilloscope (Lecroy WP760Zi) was set to 2-channel mode, which increased the

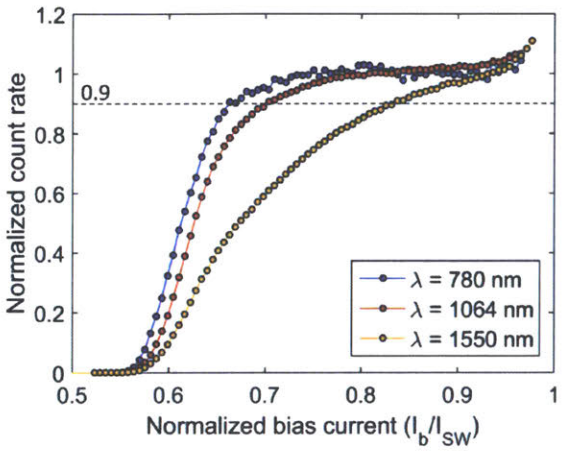

Figure 4-13: Count rate vs. bias current curves for different photon energies. With increasing photon energy, the detector showed more prominent saturation behavior. The S parameters are 0.17 ($\lambda = 1550\,\text{nm}$), 0.30 ($\lambda = 1064\,\text{nm}$), and 0.33 ($\lambda = 780\,\text{nm}$). (Device number: SPE775-4A4; temperature: 2.45 K. I_{SW}= 17 μA.)

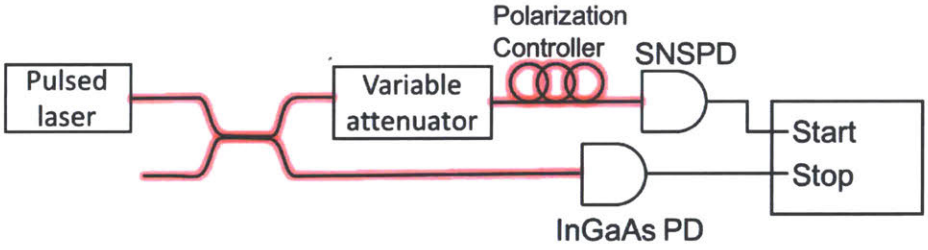

Figure 4-14: Schematic of the setup for jitter measurement.

sample rate to 40 GS/s. We triggered at SNSPD pulse ("start" signal), and measure the time delay for the InGaAs photodetector pulse ("stop" signal). We set the trigger levels (positive edge trigger) for both channels to be 50% of the corresponding pulse height.

Figure 4-15 shows the instrument response function (IRF). The detector was biased at $\sim 0.92\% I_{\text{SW}}$. The histogram was from a set of 50,000 data points, and the time bin was 1 ps. We fit the IRF using a Gaussian function, and found the full-width half-maximum (FWHM) jitter to be 52 ps.

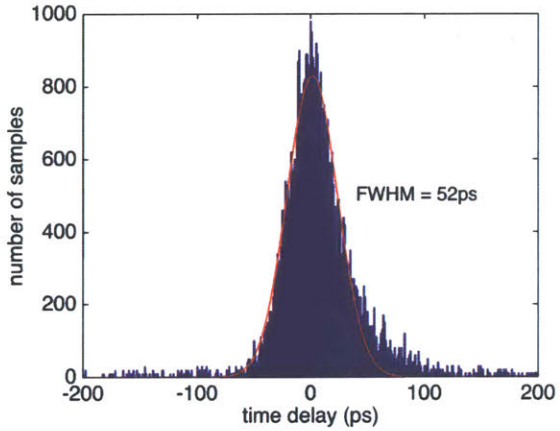

Figure 4-15: Instrument response function of the detector. A Gaussian fit reveals a FWHM jitter of 52 ps. (Device number: SPE775-4A4; temperature: 2.45 K; wavelength: 1.55 μm.)

Chapter 5

Conclusion and Future Work

In this thesis, we developed a complete fabrication process for making high-performance SNSPDs on AlN, and demonstrated their integration with AlN photonic waveguides. The detectors fabricated on this new substrate material showed saturated detection efficiency from visible to near-IR, sub-60-ps timing jitter, and $\sim$6 ns reset time.

With recent advances in photonic integrated single-photon sources and quantum memories [45], this thesis work will contribute to achieving a fully integrated quantum photonic processor.

As the next step, we will characterize the on-chip detection efficiency of the integrated detectors. At the same time, we will integrate single-photon source in diamond membranes to the AlN photonic chip, and perform on-chip single photon detection, as depicted in Fig. 2-1 and Fig. 2-2. The high quantum efficiency and low timing jitter of our detectors should enable more accurate photon correlation measurement.

Another effort that I am currently making is to develop large array of integrated detectors. Inspired of the recently demonstrated transmission-line-based superconducting nanowire single-photon imager [21], we are trying to implement similar architecture on AlN waveguide system. Figure 5-1 shows the proposed single-photon detector array on PIC for photonic quantum walk detection. Photons are injected into one of the channels in an waveguide array, undergo random walk, and get detected by the on-chip detectors. The detectors are connected through slow-wave transmission delay lines; the electrical pulses generated from different sites can be distinguished by

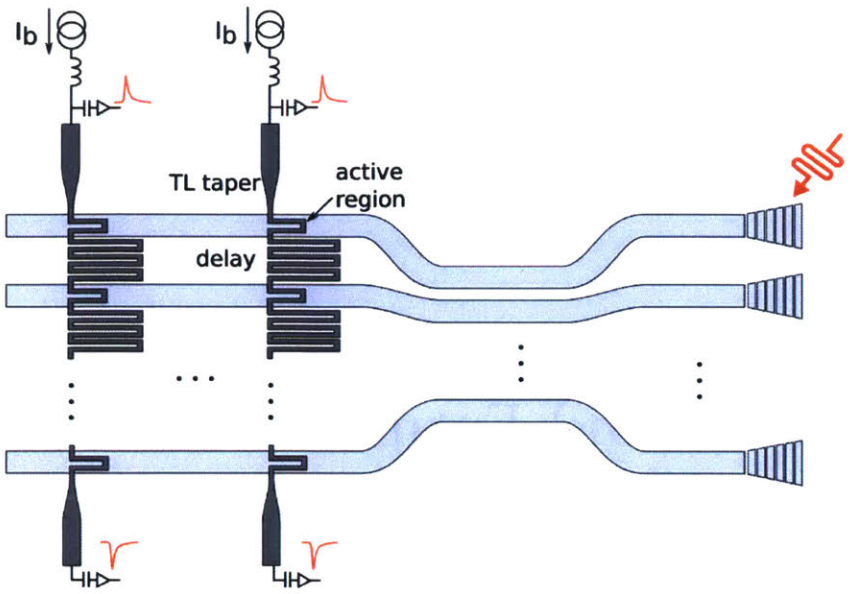

Figure 5-1: A proposed single-photon detector array on PIC for quantum walk detection.

the timing differences registered on the two readout ends.

On the understanding of device physics in the SNSPDs, many intriguing problems are worth investigating. For example, what is the ultimate timing jitter of these detectors, and what limits it? What could be the ultimate speed limit, and is there any way to circumvent it? And some questions are related directly to SNSPDs on AlN, including how surface roughness affects detector performance, what exactly the thermal boundary conductance between NbN and AlN is and how it affects our devices, what limits the switching currents from getting the actual depairing currents, etc. Understanding the underlying physics will guide the engineering of the devices, and drastically push forward the detector performance.

Finally, by exploiting the piezoelectric and electro-optical properties of AlN, and combining them with superconducting electronics, one may potentially realize fast on-chip optical modulation and feed-forward operations.

Appendix A

Probe Station Fiber Output Profile Calibration

This appendix describes the optical calibration of the Lake Shore cryogenic probe station. In the probe station, the detector chips are illuminated from the backside using probing fiber. The probing fiber has a relatively large NA so it can illuminate larger area of the chip (Thorlabs UHNA3).

The output beam profile from a fiber tip follows a Gaussian distribution with a diverging angle, which can be described as follows:

$$P_x(x,z) = P_{0_x} e^{-0.5\left(\frac{x-x_0}{W_x(z)}\right)^2}$$

$$P_y(y,z) = P_{0_y} e^{-0.5\left(\frac{y-y_0}{W_y(z)}\right)^2}$$

where the x-y plane is perpendicular to the axial direction of the fiber; x_0 and y_0 denote the center position of the 2-D Gaussian profile; $P_{x/y}$ is the optical power density distribution along x/y axis.

A beam profiler (Thorlabs BP109-IR2) was used to measure the profile of the output beam at different distances (see Fig. A-1 for the experimental setup). The fiber tip was fixed, and the beam profiler moved away from the fiber tip along the optical rail from 280 mm to 300 mm (readings from the ruler of the optical rail) in step of 1 mm. For each z position, 10 measurements were recorded. The probing

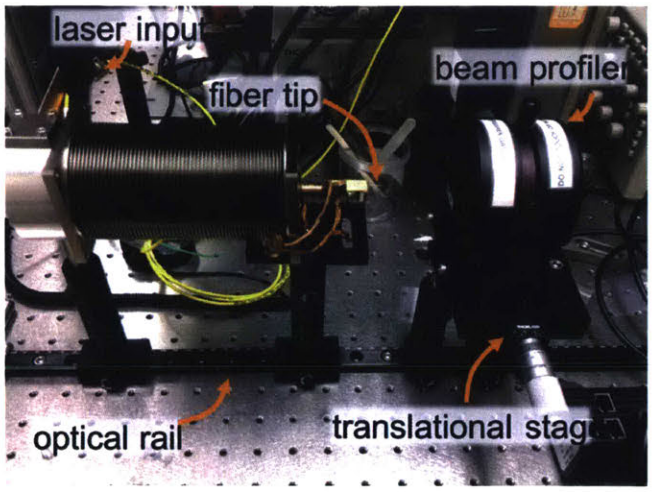

Figure A-1: The setup to calibrate the beam profile coming out from the probing fiber.

fiber was connected to a mode-locked laser with center wavelength of 1550 nm, and an optical powermeter (photodetector: Thorlabs S122C; powermeter: PM100D) was used to measure the transmission.

The total loss for the probing fiber was 3.42 dB, i.e., 45.4% transmission. The relatively large loss was because of the mismatch of the patch cable (SMF-28) and probing fiber (UHNA3).

Figure A-2 shows a typical Gaussian beam profile (x direction) measured at z = 290 mm.

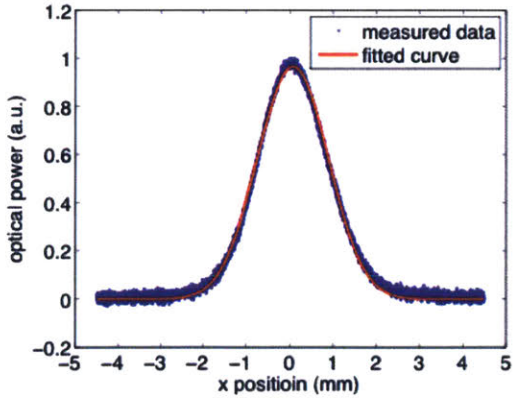

Figure A-2: Gaussian beam profile along x direction measured at z = 290 mm

Each measurement was fitted using Gaussian interpolation, where x_0, W_x, P_{0_x},

y_0, W_y and P_{0_y} were extracted. A clip (filter) of 0.13 is used to reduce the effect of noise (i.e., power values less than 0.13 of the maximum power is not used for curve fitting).

Figure A-3 shows W_x and W_y as a function of z. Fitting them using linear regression, we have

$$W_x(z) = 0.0507(z - 268)[\text{mm}]$$

$$W_y(z) = 0.0540(z - 269)[\text{mm}]$$

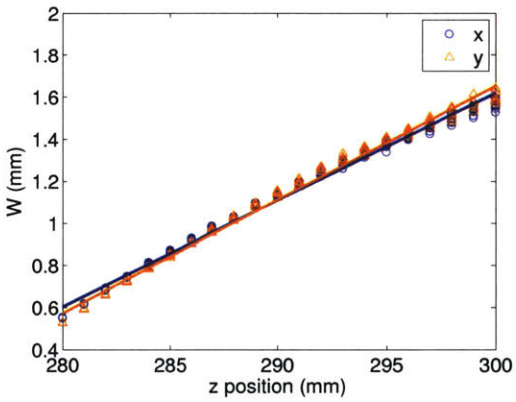

Figure A-3: W_x and W_y as a function of z

Our measurement suggests that the numerical aperture (measured at 1% power) for the fiber is $NA \approx \sin(\arctan(\frac{0.0507+0.0540}{2} \times \sqrt{-2\ln(0.01)})) = 0.157$. This value is significantly smaller than the nominal value of 0.35.

In the probe station, we measured the distance from the fiber tip to the sample holder using a caliper, and found it to be 9.5 mm. Knowing the distance and beam profile, we can then calculate the photon intensity on the detector.

Bibliography

[1] R. Hadfield, "Single-photon detectors for optical quantum information applications," *Nat. Photonics*, vol. 3, no. 12, pp. 696–705, 2009.

[2] A. D. Semenov, G. N. Gol tsman, and R. Sobolewski, "Hot-electron effect in superconductors and its applications for radiation sensors," *Supercond. Sci. Technol.*, vol. 15, no. 4, pp. R1–R16, 2002.

[3] H.-L. Yin, T.-Y. Chen, Z.-W. Yu, H. Liu, L.-X. You, Y.-H. Zhou, S.-J. Chen, Y. Mao, M.-Q. Huang, W.-J. Zhang, H. Chen, M. J. Li, D. Nolan, F. Zhou, X. Jiang, Z. Wang, Q. Zhang, X.-B. Wang, and J.-W. Pan, "Measurement-Device-Independent Quantum Key Distribution Over a 404 km Optical Fiber," *Phys. Rev. Lett.*, vol. 117, no. 19, p. 190501, nov 2016.

[4] M. Shaw, K. Birnbaum, M. Cheng, M. Srinivasan, K. Quirk, J. Kovalik, A. Biswas, A. D. Beyer, F. Marsili, V. Verma, R. P. Mirin, S. W. Nam, J. A. Stern, and W. H. Farr, "A Receiver for the Lunar Laser Communication Demonstration Using the Optical Communications Telescope Laboratory," in *CLEO 2014*. Washington, D.C.: OSA, 2014, p. SM4J.2.

[5] L. K. Shalm, E. Meyer-Scott, B. G. Christensen, P. Bierhorst, M. A. Wayne, M. J. Stevens, T. Gerrits, S. Glancy, D. R. Hamel, M. S. Allman, K. J. Coakley, S. D. Dyer, C. Hodge, A. E. Lita, V. B. Verma, C. Lambrocco, E. Tortorici, A. L. Migdall, Y. Zhang, D. R. Kumor, W. H. Farr, F. Marsili, M. D. Shaw, J. A. Stern, C. Abellan, W. Amaya, V. Pruneri, T. Jennewein, M. W. Mitchell, P. G. Kwiat, J. C. Bienfang, R. P. Mirin, E. Knill, and S. W. Nam, "Strong Loophole-Free Test of Local Realism," *Phys. Rev. Lett.*, vol. 115, no. 25, pp. 1–10, 2015.

[6] G. N. Gol'tsman, O. Okunev, G. Chulkova, A. Lipatov, A. Semenov, K. Smirnov, B. Voronov, A. Dzardanov, C. Williams, and R. Sobolewski, "Picosecond superconducting single-photon optical detector," *Appl. Phys. Lett.*, vol. 79, no. 6, pp. 705–707, 2001.

[7] J. J. Renema, R. Gaudio, Q. Wang, Z. Zhou, A. Gaggero, F. Mattioli, R. Leoni, D. Sahin, M. J. A. de Dood, A. Fiore, and M. P. van Exter, "Experimental Test of Theories of the Detection Mechanism in a Nanowire Superconducting Single Photon Detector," *Phys. Rev. Lett.*, vol. 112, no. 11, p. 117604, 2014.

[8] A. G. Kozorezov, C. Lambert, F. Marsili, M. J. Stevens, V. B. Verma, J. A. Stern, R. Horansky, S. Dyer, S. Duff, D. P. Pappas, A. Lita, M. D. Shaw, R. P. Mirin, and S. W. Nam, "Quasiparticle recombination in hotspots in superconducting current-carrying nanowires," *Phys. Rev. B*, vol. 92, no. 6, p. 064504, 2015.

[9] A. Engel, J. J. Renema, K. Il'in, and A. Semenov, "Detection mechanism of superconducting nanowire single-photon detectors," *Supercond. Sci. Technol.*, vol. 28, no. 11, p. 114003, 2015.

[10] J. R. Clem and K. K. Berggren, "Geometry-dependent critical currents in superconducting nanocircuits," *Phys. Rev. B - Condens. Matter Mater. Phys.*, vol. 84, no. 17, pp. 1–27, 2011.

[11] V. Anant, A. J. Kerman, E. A. Dauler, J. K. W. Yang, K. M. Rosfjord, and K. K. Berggren, "Optical properties of superconducting nanowire single-photon detectors," *Opt. Express*, vol. 16, no. 14, p. 10750, 2008.

[12] F. Marsili, V. B. Verma, J. a. Stern, S. Harrington, a. E. Lita, T. Gerrits, I. Vayshenker, B. Baek, M. D. Shaw, R. P. Mirin, and S. W. Nam, "Detecting Single Infrared Photons with 93% System Efficiency," *Nat. Photonics*, vol. 7, no. 3, pp. 210–214, 2013.

[13] M. K. Akhlaghi, E. Schelew, and J. F. Young, "Waveguide integrated superconducting single-photon detectors implemented as near-perfect absorbers of coherent radiation," *Nat. Commun.*, vol. 6, p. 8233, 2015.

[14] M. K. Akhlaghi and A. H. Majedi, "Gated mode superconducting nanowire single photon detectors," *Opt. Express*, vol. 20, no. 2, p. 1608, 2012.

[15] A. J. Kerman, E. A. Dauler, and B. S. Robinson, "Superconducting nanowire photon-counting detectors for optical communications," *Lincoln Lab. J.*, vol. 16, no. 1, pp. 217–224, 2006.

[16] A. Vetter, S. Ferrari, P. Rath, R. Alaee, O. Kahl, V. Kovalyuk, S. Diewald, G. N. Goltsman, A. Korneev, C. Rockstuhl, and W. H. P. Pernice, "Cavity-Enhanced and Ultrafast Superconducting Single-Photon Detectors," *Nano Lett.*, vol. 16, no. 11, pp. 7085–7092, nov 2016.

[17] M. Ejrnaes, R. Cristiano, O. Quaranta, S. Pagano, and A. Gaggero, "A cascade switching superconducting single photon detector A cascade switching superconducting single photon detector," *Appl. Phys. Lett.*, vol. 262509, no. 26, p. 262509, dec 2007.

[18] H. Shibata, K. Shimizu, H. Takesue, and Y. Tokura, "Ultimate low system dark-count rate for superconducting nanowire single-photon detector." *Opt. Lett.*, vol. 40, no. 14, pp. 3428–31, jul 2015.

[19] C. M. Natarajan, M. G. Tanner, and R. H. Hadfield, "Superconducting nanowire single-photon detectors: physics and applications," *Supercond. Sci. Technol.*, vol. 25, no. 6, p. 063001, 2012.

[20] N. Calandri, Q.-Y. Zhao, D. Zhu, A. Dane, and K. K. Berggren, "Superconducting nanowire detector jitter limited by detector geometry," *Appl. Phys. Lett.*, vol. 109, no. 15, p. 152601, oct 2016.

[21] Q.-Y. Zhao, D. Zhu, N. Calandri, A. E. Dane, A. N. McCaughan, F. Bellei, H.-Z. Wang, D. F. Santavicca, and K. K. Berggren, "A Single-Photon Imager Based on Microwave Plasmonic Superconducting Nanowire," *arXiv:1605.08693*, may 2016.

[22] X. Hu, T. Zhong, J. E. White, E. a. Dauler, F. Najafi, C. H. Herder, F. N. C. Wong, and K. K. Berggren, "Fiber-coupled nanowire photon counter at 1550 nm with 24% system detection efficiency." *Opt. Lett.*, vol. 34, no. 23, pp. 3607–3609, 2009.

[23] S. Miki, T. Yamashita, M. Fujiwara, M. Sasaki, and Z. Wang, "Multichannel SNSPD system with high detection efficiency at telecommunication wavelength," *Opt. Lett.*, vol. 35, no. 13, p. 2133, jul 2010.

[24] A. J. Miller, A. E. Lita, B. Calkins, I. Vayshenker, S. M. Gruber, and S. W. Nam, "Compact cryogenic self-aligning fiber-to-detector coupling with losses below one percent," *Opt. Express*, vol. 19, no. 10, p. 9102, may 2011.

[25] F. Bellei, A. P. Cartwright, A. N. McCaughan, A. E. Dane, F. Najafi, Q. Zhao, and K. K. Berggren, "Free-space-coupled superconducting nanowire single-photon detectors for infrared optical communications," *Opt. Express*, vol. 24, no. 4, p. 3248, 2016.

[26] J. P. Sprengers, A. Gaggero, D. Sahin, S. Jahanmirinejad, G. Frucci, F. Mattioli, R. Leoni, J. Beetz, M. Lermer, M. Kamp, S. HoÌĹfling, R. Sanjines, and A. Fiore, "Waveguide superconducting single-photon detectors for integrated quantum photonic circuits," *Appl. Phys. Lett.*, vol. 99, no. 18, p. 181110, nov 2011.

[27] W. Pernice, C. Schuck, O. Minaeva, M. Li, G. Goltsman, a.V. Sergienko, and H. Tang, "High-speed and high-efficiency travelling wave single-photon detectors embedded in nanophotonic circuits," *Nat. Commun.*, vol. 3, p. 1325, 2012.

[28] G. Reithmaier, M. Kaniber, F. Flassig, S. Lichtmannecker, K. Müller, A. Andrejew, J. Vučković, R. Gross, and J. J. Finley, "On-Chip Generation, Routing, and Detection of Resonance Fluorescence," *Nano Lett.*, vol. 15, no. 8, pp. 5208–5213, 2015.

[29] C. Schuck, W. H. P. Pernice, and H. X. Tang, "NbTiN superconducting nanowire detectors for visible and telecom wavelengths single photon counting on Si3N4 photonic circuits," *Appl. Phys. Lett.*, vol. 102, no. 5, 2013.

[30] F. Najafi, J. Mower, N. C. Harris, F. Bellei, A. Dane, C. Lee, X. Hu, P. Kharel, F. Marsili, S. Assefa, K. K. Berggren, and D. Englund, "On-chip detection of non-classical light by scalable integration of single-photon detectors," *Nat. Commun.*, vol. 6, pp. 1–8, 2015.

[31] P. Rath, O. Kahl, S. Ferrari, F. Sproll, G. Lewes-Malandrakis, D. Brink, K. Ilin, M. Siegel, C. Nebel, and W. Pernice, "Superconducting single photon detectors integrated with diamond nanophotonic circuits," *arXiv:1505.04251*, p. 28, may 2015.

[32] H. A. Atikian, A. Eftekharian, A. Jafari Salim, M. J. Burek, J. T. Choy, A. Hamed Majedi, and M. Lončar, "Superconducting nanowire single photon detector on diamond," *Appl. Phys. Lett.*, vol. 104, no. 12, p. 122602, mar 2014.

[33] P. Kok, W. J. Munro, K. Nemoto, T. C. Ralph, J. P. Dowling, and G. J. Milburn, "Linear optical quantum computing with photonic qubits," *Rev. Mod. Phys.*, vol. 79, no. 1, pp. 135–174, 2007.

[34] V. B. Verma, B. Korzh, F. Bussières, R. D. Horansky, S. D. Dyer, A. E. Lita, I. Vayshenker, F. Marsili, M. D. Shaw, H. Zbinden, R. P. Mirin, and S. W. Nam, "High-efficiency superconducting nanowire single-photon detectors fabricated from MoSi thin-films," *Opt. Express*, vol. 23, no. 26, p. 33792, dec 2015.

[35] F. Najafi, A. Dane, F. Bellei, Q. Zhao, K. a. Sunter, A. N. McCaughan, and K. K. Berggren, "Fabrication process yielding saturated nanowire single-photon detectors with 24-ps jitter," *IEEE J. Sel. Top. Quantum Electron.*, vol. 21, no. 2, pp. 1–7, 2015.

[36] O. Kahl, W. Pernice, O. Kahl, S. Ferrari, P. Rath, A. Vetter, and C. Nebel, "High efficiency, on-chip single-photon detection for diamond nanophotonic circuits," *J. Light. Technol.*, vol. 8724, no. c, pp. 1–1, 2015.

[37] M. G. Tanner, L. S. E. Alvarez, W. Jiang, R. J. Warburton, Z. H. Barber, and R. H. Hadfield, "A superconducting nanowire single photon detector on lithium niobate." *Nanotechnology*, vol. 23, no. 50, p. 505201, dec 2012.

[38] A. N. McCaughan and K. K. Berggren, "A superconducting-nanowire three-terminal electrothermal device." *Nano Lett.*, vol. 14, no. 10, pp. 5748–53, 2014.

[39] A. N. McCaughan, N. S. Abebe, Q.-Y. Zhao, and K. K. Berggren, "Using Geometry To Sense Current," *Nano Lett.*, vol. 16, no. 12, pp. 7626–7631, dec 2016.

[40] S. Doerner, A. Kuzmin, S. Wuensch, I. Charaev, and M. Siegel, "Operation of Multi-Pixel Radio-Frequency Superconducting Nanowire Single-Photon Detector Arrays," *IEEE Trans. Appl. Supercond.*, vol. 27, no. 4, p. 2201005, 2016.

[41] K. Yoshida, T. Uchida, S. Nishioka, Y. Kanda, and S. Kohjiro, "Design and performance of a velocity-matched broadband optical modulator with superconducting electrodes," *IEEE Trans. Appiled Supercond.*, vol. 9, no. 2, pp. 3421–3424, jun 1999.

[42] C. Schuck, X. Guo, L. Fan, X.-S. Ma, M. Poot, and H. X. Tang, "Quantum interference in heterogeneous superconducting-photonic circuits on a silicon chip," *Nat. Commun.*, vol. 7, p. 11, nov 2015.

[43] C. Xiong, W. H. P. Pernice, and H. X. Tang, "Low-loss, silicon integrated, aluminum nitride photonic circuits and their use for electro-optic signal processing." *Nano Lett.*, vol. 12, no. 7, pp. 3562–8, jul 2012.

[44] C. Xiong, W. H. P. Pernice, X. Sun, C. Schuck, K. Y. Fong, and H. X. Tang, "Aluminum nitride as a new material for chip-scale optomechanics and nonlinear optics," *New J. Phys.*, vol. 14, 2012.

[45] S. L. Mouradian, T. Schröder, C. B. Poitras, L. Li, J. Goldstein, E. H. Chen, M. Walsh, J. Cardenas, M. L. Markham, D. J. Twitchen, M. Lipson, and D. Englund, "Scalable Integration of Long-Lived Quantum Memories into a Photonic Circuit," *Phys. Rev. X*, vol. 5, no. 3, p. 31009, jul 2015.

[46] J. K. W. Yang, A. J. Kerman, E. A. Dauler, V. Anant, K. M. Rosfjord, and K. K. Berggren, "Modeling the electrical and thermal response of superconducting nanowire single-photon detectors," *IEEE Trans. Appl. Supercond.*, vol. 17, no. 2, pp. 558–581, 2007.

[47] F. Marsili, F. Najafi, C. Herder, and K. K. Berggren, "Electrothermal simulation of superconducting nanowire avalanche photodetectors," *Appl. Phys. Lett.*, vol. 98, no. 9, pp. 19–22, mar 2011.

[48] F. Najafi, F. Marsili, E. Dauler, R. J. Molnar, and K. K. Berggren, "Timing performance of 30-nm-wide superconducting nanowire avalanche photodetectors," *Appl. Phys. Lett.*, vol. 100, no. 15, pp. 1–5, 2012.

[49] F. Marsili, F. Najafi, E. Dauler, R. J. Molnar, and K. K. Berggren, "Afterpulsing and instability in superconducting nanowire avalanche photodetectors," *Appl. Phys. Lett.*, vol. 100, no. 11, pp. 1–6, 2012.

[50] A. D. Semenov, R. S. Nebosis, M. A. Heusinger, and K. F. Renk, "Two-temperature model of nonequilibrium photoresponse of superconducting films to pulsed radiation," *Phys. C Supercond. its Appl.*, vol. 235-240, no. PART 3, pp. 1971–1972, 1994.

[51] A. D. Semenov, G. N. Gol'tsman, and A. a. Korneev, "Quantum detection by current carrying superconducting film," *Phys. C Supercond. its Appl.*, vol. 351, no. 4, pp. 349–356, 2001.

[52] A. Kamlapure, M. Mondal, M. Chand, A. Mishra, J. Jesudasan, V. Bagwe, L. Benfatto, V. Tripathi, and P. Raychaudhuri, "Measurement of magnetic penetration depth and superconducting energy gap in very thin epitaxial NbN films," *Appl. Phys. Lett.*, vol. 96, no. 7, pp. 2–5, 2010.

[53] W. J. Skocpol, M. R. Beasley, and M. Tinkham, "Self-heating hotspots in superconducting thin-film microbridges," *J. Appl. Phys.*, vol. 45, no. 9, p. 4054, 1974.

[54] T. P. Orlando, K. a. Delin, and C. J. Lobb, "Foundations of Applied Superconductivity," p. 109, 1991.

[55] E. J. Zeman and G. C. Schatz, "An accurate electromagnetic theory study of surface enhancement factors for silver, gold, copper, lithium, sodium, aluminum, gallium, indium, zinc, and cadmium," *J. Phys. Chem.*, vol. 91, no. 3, pp. 634–643, 1987.

[56] M. Staffaroni, J. Conway, S. Vedantam, J. Tang, and E. Yablonovitch, "Circuit analysis in metal-optics," *Photonics Nanostructures - Fundam. Appl.*, vol. 10, no. 1, pp. 166–176, jan 2012.

[57] D. Zhu, M. Bosman, and J. K. W. Yang, "A circuit model for plasmonic resonators." *Opt. Express*, vol. 22, no. 8, pp. 9809–19, apr 2014.

[58] J. Zmuidzinas, "Superconducting Microresonators: Physics and Applications," *Annu. Rev. Condens. Matter Phys.*, vol. 3, no. 1, pp. 169–214, 2012.

[59] D. C. Mattis and J. Bardeen, "Theory of the anomalous skin effect in normal and superconducting metals," *Phys. Rev.*, vol. 111, no. 2, pp. 412–417, 1958.

[60] J. C. Swihart, "Field Solution for a Thin-Film Superconducting Strip Transmission Line," *J. Appl. Phys.*, vol. 32, no. 3, p. 461, jun 1961.

[61] A. Semenov, B. Günther, U. Böttger, H.-W. Hübers, H. Bartolf, A. Engel, A. Schilling, K. Ilin, M. Siegel, R. Schneider, D. Gerthsen, and N. A. Gippius, "Optical and transport properties of ultrathin NbN films and nanostructures," *Phys. Rev. B*, vol. 80, no. 5, p. 054510, aug 2009.

[62] W. D. Gregory, "Superconducting Transition Width in Pure Gallium Single Crystals," *Phys. Rev.*, vol. 165, no. 2, pp. 556–561, jan 1968.

[63] S. Shetty, J. Ghatak, and S. Shivaprasad, "Surface nitridation induced AlN nanocolumnar growth on c-sapphire," *Solid State Commun.*, vol. 180, pp. 7–10, 2014.

[64] A. N. McCaughan, Q. Zhao, and K. K. Berggren, "nanoSQUID operation using kinetic rather than magnetic induction," *Sci. Rep.*, vol. 6, p. 28095, jun 2016.

[65] J. K. W. Yang and K. K. Berggren, "Using high-contrast salty development of hydrogen silsesquioxane for sub-10-nm half-pitch lithography," *J. Vac. Sci. Technol. B Microelectron. Nanom. Struct.*, vol. 25, no. 6, p. 2025, 2007.

[66] F. Marsili, F. Najafi, E. Dauler, F. Bellei, X. Hu, M. Csete, R. J. Molnar, and K. K. Berggren, "Single-photon detectors based on ultranarrow superconducting nanowires," *Nano Lett.*, vol. 11, no. 5, pp. 2048–2053, 2011.